The formation and evolution of the supraglacial weathering crust on the Greenland Ice Sheet

Journal:	*Journal of Glaciology*
Manuscript ID	Draft
Manuscript Type:	Article
Date Submitted by the Author:	n/a
Complete List of Authors:	Stevens, Ian; Aarhus University, Environmental Science; GEUS, Glaciology and Cliimate Cook, Joseph; Aarhus University, Environmental Science Chevrollier, Lou-Anne; Aarhus University, Environmental Sciences Hepburn, Adam; Aberystwyth University, Department of Geography and Earth Sciences Anesio, Alexandre; Aarhus University, Department of Environmental Sciences Benning, Liane; GFZ Helmholtz Centre for Geosciences, Inferface Geochemistry Section; Freie Universität Berlin, Department of Earth Science Tranter, Martyn; Aarhus University, Environmental Sciences
Keywords:	Melt - surface, Glacier ablation phenomena, Glaciological model experiments, Snow/ice surface processes
Abstract:	The near-surface weathering crust is a thin (< 0.5 m), low density ice layer that develops on glacier surfaces during the ablation season and is formed by internal melting driven by the penetration of shortwave radiation into polycrystalline glacier ice. This ‘photic zone’ hosts microbial communities, mediates biogeochemical processes, and routes meltwater to the channelised supraglacial drainage network. Despite these critical roles, direct field measurements of weathering crust formation and evolution are scarce – rather, current understanding is largely derived from modelling approaches. Here, we present in-situ measurements of

weathering crust density at five sites on the western Greenland Ice Sheet, each over a 19 – 25-hour period. Shallow ice cores revealed weathering crust ice densities of 420 – 910 kg m-3, demonstrating dynamic evolution of the weathering crust linked to diurnal shortwave radiation receipt. We compare our empirical data with two existing weathering crust models, neither of which fully reproduce the observed ice density or its temporal variability. Additionally, we reveal that the density of the uppermost 0.1 m of the weathering crust is a key control on bare-ice albedo. Our findings highlight the need for improved process-level-understanding and parameterisations of weathering crust dynamics in surface energy balance models.

The formation and evolution of the supraglacial weathering crust on the Greenland Ice Sheet

Ian T. Stevens[1,2]*, Joseph M. Cook[1], Lou-Anne Chevrollier[1], Adam J. Hepburn[3], Alexandre M. Anesio[1], Liane G. Benning[4,5], and Martyn Tranter[1]

1. Department of Environmental Science, Aarhus University, Denmark
2. Department of Glaciology and Climate, GEUS, Denmark
3. Department of Geography and Earth Sciences, Aberystwyth University, UK
4. Interface Geochemistry Section, GFZ, Helmholtz Centre for Geosciences, Potsdam, Germany
5. Department of Earth Science, Freie Universität Berlin, Germany

*corresponding author: iaste@geus.dk

Abstract

The near-surface weathering crust is a thin (< 0.5 m), low density ice layer that develops on glacier surfaces during the ablation season and is formed by internal melting driven by the penetration of shortwave radiation into polycrystalline glacier ice. This ‘photic zone’ hosts microbial communities, mediates biogeochemical processes, and routes meltwater to the channelised supraglacial drainage network. Despite these critical roles, direct field measurements of weathering crust formation and evolution are scarce – rather, current understanding is largely derived from modelling approaches. Here, we present *in situ* measurements of weathering crust density at five sites on the western Greenland Ice Sheet, each over a 19 – 25-hour period. Shallow ice cores revealed weathering crust ice densities of 420 – 910 kg m^{-3}, demonstrating dynamic evolution of the weathering crust linked to diurnal shortwave radiation receipt. We compare our empirical data with two existing weathering crust models, neither of which fully reproduce the observed ice density or its temporal variability. Additionally, we reveal that the density of the uppermost 0.1 m of the weathering crust is a key control on bare-ice albedo. Our findings highlight the need for improved process-level-understanding and parameterisations of weathering crust dynamics in surface energy balance models.

1. Introduction

Contemporary climate warming is accelerating the melt rate of glaciers and ice sheets worldwide (Hugonnet and others 2021; Rounce and others 2023). Consequently, the surface area of bare-ice, and its duration of exposure is increasing (Ohmura and Boettcher 2022; Žebre and others 2021), as is meltwater production (e.g. Fettweis and others 2013; Huss and Hock 2018; Noël and others 2021). Drainage of surface meltwater is commonly characterised as occurring through an efficient, channelised system (e.g. Smith and others 2015; Chu 2014; Fountain and Walder 1998; Pitcher and Smith 2019), but this assumption has been challenged by a resurgence of interest in the supraglacial weathering crust, which forms on melting bare-ice on glaciers around the world (Hoffman and others 2014; Stevens and others 2018; Tedstone and others 2020; Yang and others 2018). The weathering crust has not been formally defined, despite a 50-plus year history of research (e.g. Müller and Keeler 1969, Derikx, 1973). Herein, we define the weathering crust as: *near-surface glacier ice which has melted internally and has a bulk density ≤ 910 kg m^{-3}.*

The weathering crust plays a key role in supraglacial hydrology, acting as an inter-channel ‘perched aquifer’, delaying surface runoff from the point-of-melt to supraglacial streams (Irvine-Fynn and others 2021; Smith and others 2017; Stevens and others 2018). It functions much like a soil in a terrestrial hydrological system (Derikx 1973), modulating the timing and magnitude of supraglacial water export (Yang and others 2018), generating a lag-time between peak melt and peak channel discharge (Munro 2011). Moreover, the weathering crust plays a role in glacier surface albedo, both directly (Tedstone and others 2020), and indirectly through the suspected redistribution of light absorbing particles, such as mineral sediment, black carbon, cryoconite granules, and microbes (Chevrollier and others 2022; Cook and others 2020; McCutcheon et al. 2021; Ryan and others 2018; Wientjes et al. 2011; Wientjes et al. 2012; Williamson and others 2020). The interactions between light absorbing particles and the weathering crust remains unclear (Halbach and others 2023), despite recent attempts to examine microbial transport dynamics across northern hemisphere glaciers (Irvine-Fynn and others 2021; Stevens and others 2022). The weathering crust is a ‘photic zone’ (Edwards and others 2014) hosting diverse microbial communities (Faber and others 2024; Rassner and others 2024), alongside cryoconite holes (Cook and others 2016) and is a key location for supraglacial biogeochemical cycling (e.g. Cameron and others 2012; Doting and others 2025). Despite its critical role(s) in the supraglacial system, and the recurring hypothesis that weathering crust density and porosity govern its functionality, the processes which define the rate of evolution of the weathering crust remain poorly quantified.

Formation of the weathering crust is due to internal melting which reduces bulk ice density. Internal melting is driven primarily by energy from incoming shortwave radiation (SWR), which penetrates the ice surface (LaChapelle 1959; Munro 1990; Schuster 2001), driving preferential melt along ice crystal boundaries (Nye 1991) unique to polycrystalline glacier ice (Jennings and Hambrey 2021; Mader 1992). The created pore space is exploited by conductive heat flux from relatively warm air, further reducing ice crystal cohesion (Hoffman and others 2014; Mader 1992; Nye and Frank 1973; Nye 1991) and frictional heat derived from inter-crystalline meltwater flow (Koizumi and Naruse 1994). SWR receipt is progressively absorbed or scattered in different directions as it penetrates the ice column until it becomes extinct at depths of 1 – 8 m (Cooper and others 2021; Grenfell and Perovich 1981; Greuell and Oerlemans 1989). SWR absorption and scattering for ice free from light absorbing impurities is dependent on the physical characteristics of the weathering crust, and the incident angle of the penetrating radiation (Gardner and Sharp 2010). The distribution of energy fluxes between the surface plane and the near-surface zone remains a surface energy-balance modelling problem (van Tiggelen and others 2024), with no single universally accepted value. Currently weathering crust studies use a 36:64 surface-to-near-surface ratio (e.g. Hoffman and others 2014; Woods and Hewitt 2023), but this value is based on a definition of the ‘surface’ being 0.06 m thick and only considering SWR < 800 nm (Greuell and Oerlemans 1989), which contrasts with the < 2500 nm threshold of most modern definitions and measurement equipment. Theoretically, these values provide an SWR extinction depth of ≤ 2 m in optically clear blue ice (Irvine-Fynn and Edwards 2014; Larson 1977; 1978). Absorption and scattering result in a non-linear attenuation of SWR as light penetrates the ice surface, resulting in a characteristic depth-density curve where bulk densities range from as low as ~300 kg m^{-3} to the unweathered ice density of 910 kg m^{-3} (LaChapelle 1959).

The process of weathering occurs concurrently with surface lowering, which, in addition to SWR absorbed directly at the ice surface (Greuell and Oerlemans 1989), is driven by turbulent and sensible heat fluxes (Schuster 2001). The weathering crust will (theoretically) reach a state of dynamic equilibrium given a constant energy balance over a sustained period, where the rates of internal melting and surface lowering are equal. However, such idealised conditions do not occur in the natural environment due to changing meteorological conditions and diurnal cycles. Hence, the weathering crust is constantly evolving (Cook and others 2015). During periods of cloud cover, and at night, SWR receipt is reduced compared to clear-sky conditions during the day, shifting the energy balance ratio and increasing the relative proportion of melt energy provided by turbulent fluxes (e.g. Hock 2005). Subsequently, the rate of surface lowering exceeds that of subsurface melting (Schuster 2001; Woods and Hewitt 2023), causing the weathering crust to thin. This process may be accompanied by re-freezing of meltwater and deposition of hoar frost in the weathering crust pore space, especially during periods of low air temperature and net negative sensible heat flux.

To date, there remains a paucity of field measurements of weathering crust depth-density profiles, and no measurements which document the formation and ongoing evolution of the weathering crust. The current benchmark for measurements of this type are the ten depth-density profiles provided by Cooper and others (2018), which only provide a snapshot of weathering crust condition at a single timepoint and consequently do not enable consideration of the evolution of the weathering crust. Rather than field-based studies, recent work has approached the formation and evolution of the weathering crust as a modelling problem (Woods and Hewitt 2023; 2024) – but this model lacks field evaluation against independent field measurements of near-surface ice density at a single site over time. Consequently, in this manuscript we use five ‘reset’ ice surfaces to explore the process of ice weathering from an unweathered starting condition to a fully developed weathering crust. At each site, we present depth-density curves for the evolving weathering crust at a quasi-hourly temporal resolution throughout a 25-hour period. We pair these data with meteorological measurements to evaluate the performance of Woods & Hewitt’s (2023 and

2024) model. We additionally evaluate the only other existing weathering crust model of which we are aware, which was developed in the early 2000s (Schuster, 2001). Finally, we couple measurements of surface reflectance with near-surface ice density to assess the role of weathering crust condition and broadband surface albedo at a point scale. Our observations provide a foundation for the evaluation of current weathering crust models, highlighting the need for their development to fully comprehend glacier surface energy balance, and our lack of process-level understanding of glacier melt processes.

2. Materials and methods

2.1 Experimental setup and measurement of weathering crust evolution

Field measurements were conducted at two sites on the western margin of the Greenland Ice Sheet in the summers of 2022 (c. 40 km east of Ilulissat) and 2024 (c. 2 km east of the S6 weather station on the K-Transect; Smeets and others 2018; Figure 1a). In total, five weathering crust 'reset' experiments were conducted to explore the initial formation process of the weathering crust in response to meteorological conditions. Measurement periods were targeted on clear-sky days with no rainfall, and otherwise typical summer conditions on the Greenland Ice Sheet. One experiment was conducted at ILU-22, and four at KAN-24 – S15 and WCR 1-4 respectively. The S15 experiment was conducted on Day of Year (DOY) 215 in 2022, WCR1 and 2 experiments on DOY 203 in 2024, and WCR3 and 4 on DOY 209 in 2024. Alongside the targeted reset experiments at ILU-22, opportunistic core collection was conducted between DOYs 206 and 220, on non-reset surfaces. The core processing procedure for these cores was identical to that for the cores collected within the reset experiment.

The "reset" experimental surface was created by the removal of the weathering crust. This was achieved by a) mechanically removing weathered ice and b) by manipulating the surface energy balance. At a 2 × 2 m plot with visibly 'clean' ice (i.e. with minimal surface debris, microbes, or cryoconite holes) the topmost layers of weathered ice (c. 5 cm deep) using hand tools. Subsequently, the experimental surfaces were covered with flexible solar panels for a minimum of three days (Figure 1b). The upper ~1 m of ice at each plot was assumed to be structurally homogenous. The solar panels acted as radiation blockers, preventing SWR from reaching the ice – stopping ongoing weathering – and promoting sensible heat fluxes by warming in response to absorption of SWR. Weathering of the ice surface was initiated by the removal of the solar panels (Figure 1c). The success of this approach was validated by ice density measurements immediately following the exposure of the experimental surface (see below) – with measurements indicating bulk ice densities of ~910 kg m^{-3}, equal to unweathered ice (Cuffey and Paterson 2010).

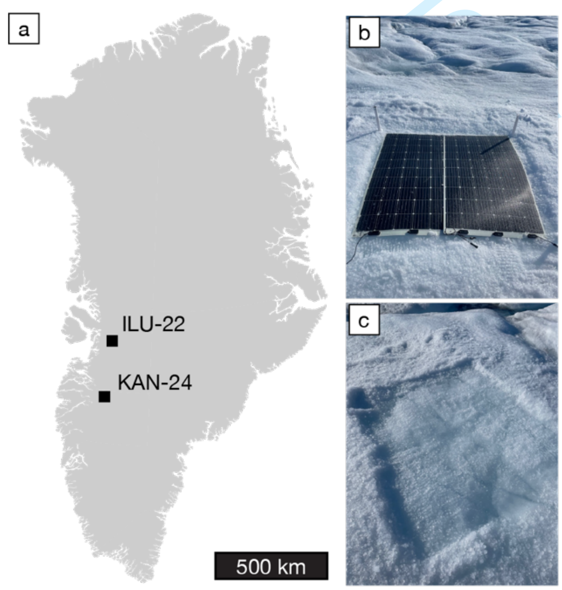

Figure 1 | a) Map of Greenland showing the location of the two field sites, and year of data collection. Panels b) and c) show the experimental setup during the 'reset' period and following surface exposure.

At each experimental plot, near-surface ice density profiles were measured over either a 19 (S15) or 25 hour (KAN-24) period between 1000 and 1100 the following day, with measurements beginning immediately after exposure of the reset surface at ~1000. Quasi-hourly measurements were collected between 1000 and 1600, and during this period depth-density profiles were paired with measurements of surface albedo. Measurements were less frequent between 1600 and 1100 – they were collected at ~1800, 2100, 0000, 0700, 0900 and 1100. Note that the S15 experiment was curtailed following the 0700 measurement, due to rainfall. This approach yielded 11 timepoints over a 19 hour period for the S15 experiment, and 12 timepoints during a 25 hour period for the four KAN-24 experiments. Albedo was measured only during the hours of 1000 and 1700, to ensure a suitable solar zenith for reliable measurements. Concurrently, hourly-averaged meteorological data were collected using either a) a custom weather station, with capabilities equivalent to that of a PROMICE station (see Fausto and others 2021, and Supplementary Table S1) in 2022, or b) the S6 weather station in the K-Transect (Smeets and others 2018) in 2024. Surface lowering between the start and end of each experimental period was measured using an ablation stake at the corner of each experimental plot.

A total of 59 depth-density density profiles were measured using a volume-gravimetry method: a ~500 mm deep core was collected using a Kovacs Mark V corer (diameter 140 mm), which was then drained of water and segmented at semi-regular intervals of ~50 mm – with respect for visual changes within the core – using a power saw. Segments were redrained, the thickness measured (digital callipers, nearest mm), and stored in pre-weighed sample bags. Core segments were weighed in a field laboratory following the cessation of the weathering period using calibrated laboratory scales (Ohaus NVT4201, 0.1 g resolution). Twenty random segments were measured three times (10 segments in 2022 and 10 segments in 2024), to determine the precision of the final bulk density measurements: ± 20 kg m^{-3}. Cores were distributed across the entirety of each 4 m^2 plot, with the maximum number of 12 cores requiring a total surface area of 0.18 m^2 (~ 4% of the total pot area).

Surface albedo of the experimental plots was measured using one of two methods, dependent upon the availability of equipment and trained personnel. In 2022, an ASD Fieldspec 4 was used with a 10° collimating lens, calibrated using a Spectralon® reflectance panel, was used. This setup provided full spectral reflectance at nanometre-scale resolution, over a 0.015 - 0.020 m^2 circular footprint, corresponding with the area required for an individual core (0.015 m^2). The exact albedo-measurement location was aligned exactly with the hourly core-site prior to core abstraction. Under the assumption of a Lambertian surface, broadband albedo was calculated by integrating the spectral reflectance using the spectral downwelling irradiance. In 2024, a Zipp and Konen CNR4 Radiometer was mounted on a tripod, and the voltage of the up/down SWR sensor was recorded using a pair of voltmeters. This setup has a larger footprint (the CNR4 is approximately semi-hemispheric, with a 150° field of view) and lower resolution (radiation between 305-2800 nm is represented with a single value), but unlike the ASD Fieldspec, it simultaneously measures incoming and outgoing SWR, and provides a 'truer' albedo, as its view angle is closer to the hemispherical view angle of the theoretical albedo definition. The same sensor is deployed on AWSs across the Greenland Ice Sheet (see Fausto and others 2021; Smeets and others 2018) and glaciers worldwide. Using this setup, albedo was measured on an undisturbed quadrant of the experimental plot, prior to core abstraction.

2.2 Model description and implementation

Field-derived depth-density profiles were used to evaluate the two weathering crust models of Schuster (2001) and Woods (and Hewitt 2023; 2024). The models function using meteorological data to calculate the relative rates of surface lowering and internal melting, outputting depth-density or depth-porosity profiles. The Schuster (2001) model evaluates the relative rates of surface lowering and internal melting, whilst the Wood (and Hewitt, 2023; 2024) model uses an enthalpy-based calculation. Both models use an extinction coefficient to define the proportion of SWR into the ice at a given depth relative to the surface. Full model descriptions can be found in the respective manuscripts and are not repeated herein in the interests of conciseness - a summary of relevant assumptions can be found in Table 1. It should be noted that neither model uses proscribed ice temperature (Table 1) – ice is either assumed to be at the melting point (Schuster 2001) or ice temperature is calculated in each model step as a function of the existing temperature and energy flux (Woods and Hewitt, 2023; 2024). Moreover, both models assume the complete absence of light-absorbing particles (i.e. they assume bare ice), and, in the case of the Woods model, the lateral advection of meltwater in the weathering crust (Cook and others 201; Stevens and others 2018; Doting and others 2025) is not incorporated. The Schuster (2001) model does not consider the presence of meltwater.

Both models were run using the field-derived meteorological data as inputs to generate depth-density curves comparable to the field measurements. Both models operate relative to the surface plane, effectively moving weathered ice 'up' the z-stack using unweathered ice from below to replace mass lost by surface lowering. Both models were run to replicate each of the reset experiments.

2.2.1 Schuster Model

We implemented the Schuster model in Python, initially using the model description in the original manuscript. The model was developed to ingest field-derived meteorological data. We strived to provide a faithful implementation of the model, but some modifications were necessary. These are as follows:

1. The original model uses a prescribed 300 second timestep. We add this as a user-defined variable to accommodate metrological datasets, which have timesteps that typically range from one minute (e.g. e.g. Maturilli 2020) to one hour (as used herein) temporal resolutions.
2. The original version uses a fixed number of layers of depths 0.01, 0.02, 0.04, 0.08, 0.16 and 0.32 m. We introduce the option to adjust the number and depth of layers in the weathering crust.
3. We prescribe an unweathered ice density of 910 kg m^{-3}, rather than 890 kg m^{-3}, as per our definition of the weathering crust and the accepted values within the literature (e.g. e.g. Cuffey and Paterson, 2010).
4. We incorporate the bulk-aerodynamic method (e.g. e.g. Braithwaite 2009; Cuffey and Paterson 2010; Oke 1987) as implemented by Brock and Arnold (2000) directly into the model, for the calculation of turbulent and latent heat fluxes.
5. In the original thesis of Schuster, the bulk extinction coefficient for SWR is defined as 0.006 m^{-1} (after Geiger 1965). However, this produces incredibly low rates of weathering and does not correspond with values reported in Geiger (1965), who use an extictnion coefficent of 0.06 cm^{-1} (equivalent to 6 m^{-1}), or the wider literature: Grenfell and Maykut (1977) suggest a value of 2 m^{-1}, whilst Woods and Hewitt (2023) used a value of 4.4 m^{-1} (conceptualised as a two-component absorption and scattering coefficient). Thus, we use a bulk SWR extinction coefficient of 6 m^{-1} – faithful to the original Geiger (1965) value, and what we assume is used in the Schuster model.
6. Certain equations in the original manuscript appear to be incomplete, and we replace the originals with new ones (Equations 1-4):

$$\mathrm{mi} = \frac{\mathrm{Q_{mi}}}{\rho_{\mathrm{ice}} \cdot \mathrm{L_f}} \quad \text{[Equation 1]}$$

$$\mathrm{ma} = \frac{\mathrm{Q_{ma}}}{\rho_{\mathrm{ice}} \cdot \mathrm{L_f}} \quad \text{[Equation 2]}$$

which become:

$$\mathrm{mi} = \mathrm{m} \cdot \left(\frac{\mathrm{Q_{mi}}}{\mathrm{m} \cdot \mathrm{L_f}}\right) \quad \text{[Equation 3]}$$

$$\mathrm{ma} = \mathrm{m} \cdot \left(\frac{\mathrm{Q_{ma}}}{\mathrm{m} \cdot \mathrm{L_f}}\right) \quad \text{[Equation 4]}$$

where *mi* and *ma* are the mass of ice lost internally and at the surface respectively, Q_{mi} and Q_{ma} are the energy available for internal and surface melting, ρ the density of ice, L_f the latent heat of fusion of ice (333.7 kJ kg^{-1} at 0 $^{\circ}$C), and *m* the initial mass of ice in the calculation layer.

2.2.2 Woods Model

The Woods model (Woods and Hewitt 2023; 2024) is publicly available and is written in MATLAB. We use the 20/12/2024 release (https://zenodo.org/records/14536244). By default, the 'continuum' Woods model represents a 100 m deep ice column as a 1D series of layers between 0.01 – 0.1 m thick, evolving according to prescribed rates of Q_{si}, (incoming SWR) and Q_o (net LWR + turbulent fluxes). Ice temperature is explicitly modelled, in contrast to the Schuster (2001) approach, and internal melting produces interstitial meltwater, which does not drain, and can refreeze in periods of negative melt energy flux (again, in contrast to the Schuster model).

To the best of our knowledge, the Woods model has not yet been forced using measured transient meteorological forcing. Here, we run the Woods model for each of our five field experiments using resampled meteorological data to derive Q_{si} and Q_o

(the latter calculated using the bulk aerodynamic method as above) and defined the surface albedo using field measurements (0.48 in 2022, 0.44 in 2024). To allow the model to equilibrate with the environmental conditions, we spinup the model over a minimum of ten hours before the first field observation. This allowed the model to reach near-surface ice temperatures corresponding to environmental conditions, which invariably reach 0 ˚C in the upper 1 m by the onset of the field measurement window (see Supplementary Information). During each spinup, Q_{si} was fixed at 0 W m^{-2}, emulating experimental conditions while ice was covered by solar panels. Our spinup also ensures that our model captures the initially unweathered ice (i.e., zero pore space, or $\Phi = 0$) , before evolving in response to transient Qsi at the start of our measurement window (corresponding to the uncovered of the ice in our field experiments). We ran the model using a 60-second timestep, linearly interpolating between the hourly measurements of Q_{si} and Q_o. The default model output is presented as pore space taken up by water, so ice density is calculated as (Equation 5):

$$\rho_{\text{bulk}} = \rho_{\text{ui}} \cdot (1 - \Phi) \quad \text{[Equation 5]}$$

where ρ_{bulk} is the bulk density of weathering crust ice, (i.e. equivalent to the field measurements), Φ is the pore space taken up by water (i.e. the Woods model output), and ρ_{ui} is the density of unweathered ice (910 kg m^{-3}).

Table 1 | Summary of model capabilities and assumptions

	Woods (2023, 2024)	Schuster (2001)
Type	Continuum enthalpy	Relative melt rate
Inputs	Q_{si} (SWR_{in})	SWR_{in}
	Q_o (LWR_{in} + turbulent fluxes [note 1])	LWR_{net}
		Turbulent fluxes [note 1]
		Air temperature
		Actual vapour pressure
		Windspeed
		Relative humidity
		Surface roughness
Outputs	Volume of air (pore space) at depth Z	Ice density at depth Z
Default constants: [note 2]		
Layer thickness (m)	0.01 [note 3]	0.01, 0.02^{n-1} [note 4]
Number of layers	1000 [note 3]	6
Initial ice density (kg m^{-3})	910	890
Extinction coefficient (m^{-1})	4.4 [note 5]	6.0
Scattering coefficient (m^{-1})	4.1338	*not applicable*
Absorption coefficient (m^{-1})	0.2637	*not applicable*
Ice temperature at depth (˚C)	-10	melt-point
Albedo	0.6	0.4
Dynamic ice temperature?	Yes	No
Pore space filled with	Meltwater	Air
Allows meltwater refreezing?	Yes	*not applicable*
Allows meltwater drainage?	No	*not applicable*
Other mass addition mechanisms?	No	No

(note 1) turbulent fluxes are calculated using the bulk aerodynamic method.
(note 2) these can be modified by the user. Changes made to these values for our model runs are described in the main text. Notably, these are layer thickness and number of layers (Schuster), initial ice density (Schuster), and albedo (both).
(note 3) in the top 10 m of the z-stack. Layer thickness increases over the full 100 m z-stack included in the model.
(note 4) where n is layer number and $2 \leq n \leq 6$.
(note 5) sum of the absorption and scattering coefficients.

3. Meteorological overview

Meteorological data and calculated sensible and latent energy fluxes are shown in Figure 2. Calculations assume that the ice is at the melting point, i.e. 0 °C. Notably, there are some periods of light cloud cover during both study periods in 2024, as indicated by the reduced periods of SWR receipt during the main daylight hours. There was a marked difference in air temperature between each observation period – S15 had the highest temperatures of 3 ± 1 °C, whilst the WCR1 & 2 period had lower temperatures (0.5 ± 0.5 °C), and the WCR3 & 4 period exhibited the lowest temperatures: almost exclusively < 0 °C and reaching as low as -4 °C. Consequently, the final period (the WCR 3 & 4 period) was one of net negative sensible heat flux. The warm air temperatures and high SWR receipt in the S15 period drove higher melt rates, and consequently more melt energy during this period was 'lost' to the latent energy flux as ice melted, than in the other observation periods.

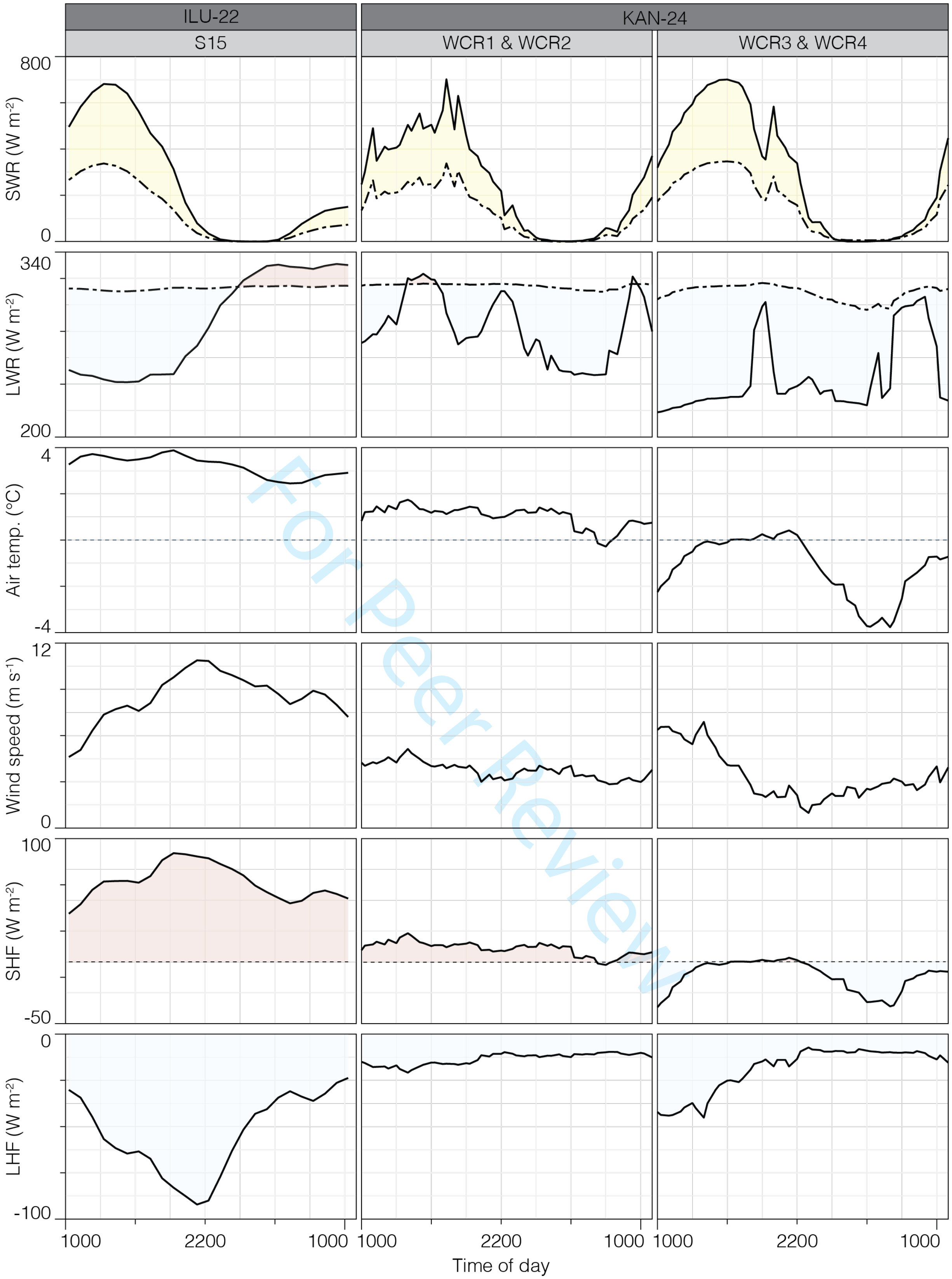

Figure 2 | Meteorological data during the three observational periods. Solid lines represent incoming energy fluxes, dash-dot lines outgoing fluxes, and dash lines are a y-axis zero-reference. Yellow shading represents net SWR receipt, while red and blue shading represents net positive or negative longwave (LWR), sensible (SHF) and latent (LHF) energy flux, respectively. SHF and LHF are modelled using the bulk-aerodynamic method (see Methods).

4. Near-Surface Ice Weathering

Our 59 depth-density curves for weathering crust ice reveal a non-linear profile (Figure 3). These profiles are as anticipated (LaChapelle, 1959), due to the non-linear absorption of SWR throughout the ice column. However, our lowest measured bulk ice density (426 kg m^{-3}) exceeds that reported by LaChapelle (1959) by over 100 kg m^{-3}, and is greater than the lowest observed density of Cooper and others (2018) by 75 kg m^{-3}. We report a maximum weathering crust depth of 0.5 m (defined as the depth when ice density ≥ 910 kg m^{-3}), which is substantially lower than the theoretical maximum of 2 m for 'optically clear ice' described by other authors (Irvine-Fynn and Edwards 2014; Larson 1977; 1978). Moreover, this depth is shallower than the field observations of Cooper and others (2018) who report weathering up to depths of 1 m. We attribute the differences in our maximal weathering crust thickness and those of other authors to three factors:

1. A potential underestimate of the SWR extinction coefficient of ice used for theoretical work, allowing for deeper SWR penetration;
2. The presence of light absorbing particles (LAPs) within the ice column, which are strong SWR absorbers (e.g. Chevrollier and others 2022; Takeuchi 2009), violating the theoretical assumption of 'optically clear ice' and;
3. The possibility that our experimental surface does not reach dynamic equilibrium with the previaling environmental conditions. For example, a measurement window longer than 25 hours may yield less dense, deeper weathering crusts. This hypothesis is supported by our own supplementary measurements form undisturbed surfaces at ILU-22, which had a lowest observed surface segment density of 339 kg m^{-3} (depth: 0 - 0.048 m), demonstrating close alignment with the minima of LaChapelle (1959) and Cooper and others (2018). However, we did not observe weathering crust depths exceeding 0.6 m.

The weathering crust exhibited a three-phase growth-decay[1] pattern during our observation periods (Figure 3). Initial growth during the day between the hours of 1000 – 1700. Throughout this period, SWR receipt was high (> ~250 W m^{-2}, Figure 2), driving internal melting (left-hand column of Figure 3). The rate of mass loss by internal melting exceeded that of surface lowering – driving rapid reduction in bulk ice density at rates of up to -80 kg m^{-3} hr^{-1} in the 0.05 m of the weathering crust closest to the surface.

The growth period was followed by a 'decay' period overnight, between 1700 – 0900. During this period, SWR receipt is low (0 to ~250 W m^{-2}, Figure 2) and internal melt rate is lower than the rate of surface lowering. However, surface lowering alone cannot entirely explain the observed decay of the weathering crust: < 0.1 m of lowering was observed throughout the entirety of each observation period, whilst ~0.2 m of lowering would be required to fully explain the effective densification of the weathering crust. Hence, additional processes are required to explain the observed crust decay – we consider that refreezing of interstitial weathering crust meltwaters and the deposition and crystallisation of hoar frost (Fierz and others 2009) may play a role. We consider refreezing of interstitial meltwater to be an implausible driver of mass accretion, due to the universally negative latent heat flux across all experiment periods – implying the melting of ice rather than the freezing of liquid water. It is, conversely, plausible that microclimates within the weathering crust drive the accretion of liquid meltwater to ice crystals from interstitial pore spaces (Hoffman and others 2014; Mader 1992; Nye and Frank 1973; Nye 1991). However, for liquid water to refreeze, it must be present – and the water table within the weathering crust is rarely < 0.1 m from the surface (Cook and others 2015; Stevens and others 2018; Stevens 2019), where apparent densification is occurring. Therefore, we attribute densification in the uppermost section of the weathering crust to hoar frost deposition, which occurs over snow and ice surfaces during periods with high relative humidity when warm air overlies a cold substrate (Horton and others 2015). Hoar deposition is possible within the unsaturated zone of the weathering crust, if air can circulate and contact exposed glacier ice crystal surfaces. Conditions were most favourable for hoar deposition during observational period S15, where air temperature and relative humidity during the decay period average 2.8 °C and 79%, respectively. In contrast, the WCR3 & 4 period had the least-favourable conditions for hoar formation, with average temperatures of -1.6 °C and relative humidity of 95 %. Notably, the S15 observations show the largest amount of decay[1], especially in the uppermost (< 0.1 m) core segments, implying the deposition of hoar frost. Nevertheless, we have no direct observations of either of these accretion processes, and further work is needed to identify their

[1] 'Growth' refers to a bulk density reduction, and 'decay' an effective bulk density increase.

presence or absence. For example, crystallographic assessments may reveal such change, as could high spatio-temporal resolution measurements of ice temperature. Ice temperature was not measured in this study due to practical limitations, and due to the primary aim of the study being to measure *in-situ* ice weathering, rather than to fully elucidate the process driving weathering crust evolution cycles.

From 0900, the weathering crust returned to a growth phase, herein termed ‘regrowth’. Note that this is only apparent in the KAN-24 experiments, and that the S15 experimental period was curtailed by the onset of light rainfall at 0930. At this time of day, the increase in solar zenith causes SWR receipt to rise and exceed 250 W m^{-2} (Figure 2). This association between weathering crust evolution and SWR receipt implies the possibility of an SWR-receipt derived ‘switch’ between growth and decay phases. However, any such threshold is dependent on the overall energy balance, which likely differs with environmental conditions (such as warmer air temperatures then we observe in this experiment), and as such we do not suggest a specific value given our small, geographically isolated, sample set. Rather, we highlight the potential for a threshold value, which requires further repetition of this work under differing environmental conditions (such as those which occur in other regions of the world), to robustly define.

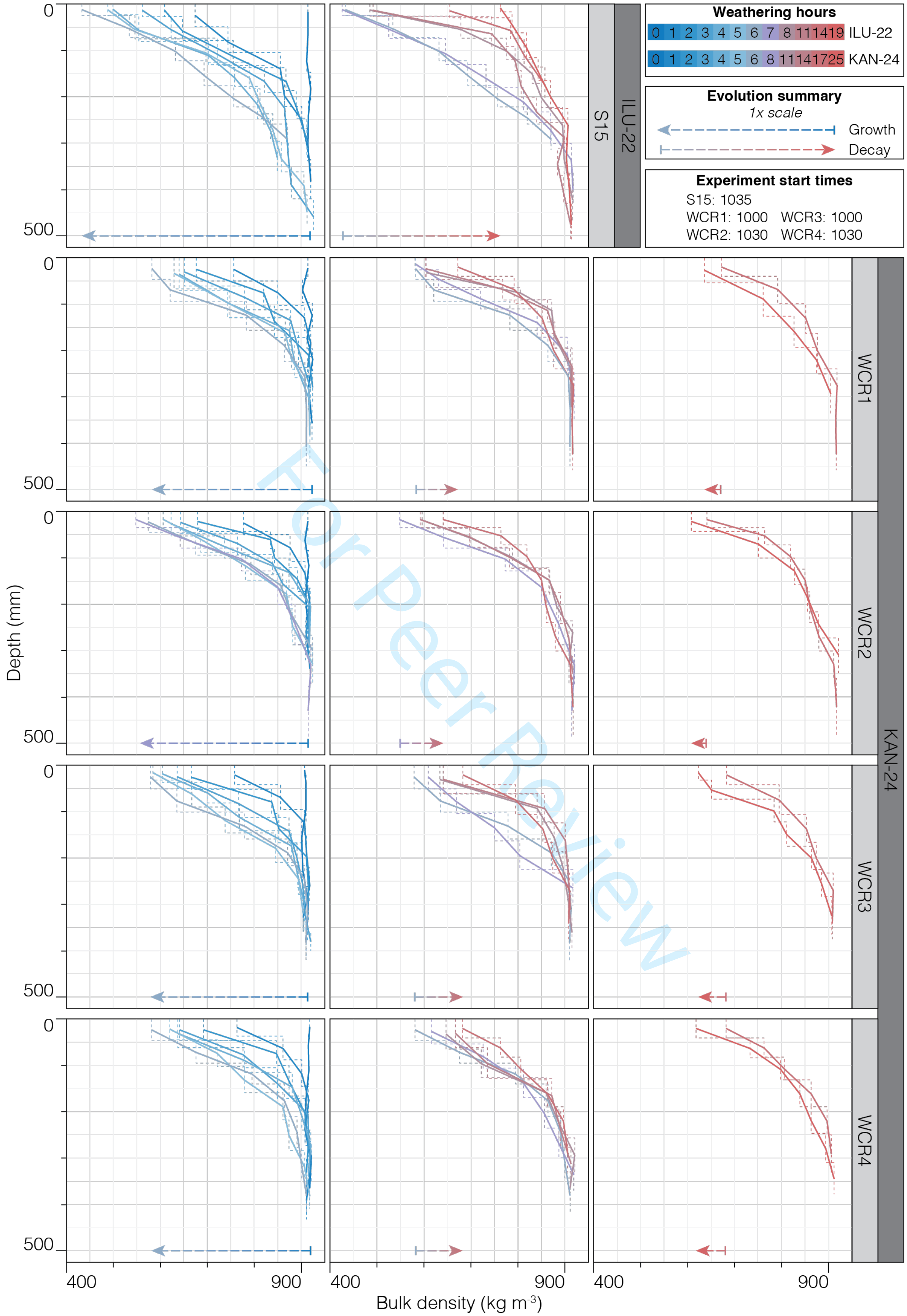

Figure 3 | Weathering crust reset experiments, showing change in ice density (y axis) across the depth profile (x axis), over time (line colour). Solid lines are interpolations of core-segment midpoints, whilst full core segment data are shown with dotted lines. The three columns indicate three separate phases of weathering crust change: left column – growth, centre column – decay, right column – regrowth (as indicated by long-dashed arrows in the plot area). Each observation period is given one row.

5. Model evaluation

The two weathering crust models (Schuster 2001; Woods and Hewitt 2023; 2024) were run to correspond with the field observation periods, using real-world meteorological data (Figures 4 and 5). The Schuster (2001) model was run using both the default segment thicknesses and a 0.01 m segment thickness, with both the default timestep and an hourly timestep. All combinations of setup parameters produced the same interpolated depth curve (Supplementary Figure 1). We use the higher resolution segment size, at a one-hour timestep for the following discussion, to enable the most appropriate comparison with our field data consisting of variable segment thicknesses and hourly meteorological measurements. The Woods (2023; 2024) model was run with the addition of measured radiative forcing but otherwise default parameters.

5.1 Field and model comparison

Firstly, we evaluate model performance by directly comparing modelled density with field density for each of the 383 core segments (Figure 6). Both models perform poorly when evaluated using this criterion. The Schuster model typically underestimates ice density when field measured density is above 800 kg m^{-3}, and overestimates density below this threshold. There is no systemic relationship between under/over prediction of density and core segment depth or field site (Figure 6). This is due to the Schuster model generating a greater degree of weathering deep within the ice column than is observed in the field data, and *vice versa*. The Woods model underestimates the degree of weathering in all model runs (Figure 6), producing shallow weathering crusts with higher bulk ice densities than either the field measurements or Schuster model (Figures 3-5). This behaviour corresponds with Woods and Hewitt's (2024) own reporting of their model (see Figure 9 in Woods and Hewitt 2024, p17) when using seasonal-like sinusoidal forcings of SWR, LWR, and turbulent fluxes.

Secondly, we evaluate the ability of the models to capture the growth-decay-growth evolution pattern observed in the field experiments. Both models capture the initial weathering crust growth phase, but neither model captures the overnight decay phase (c.f. Figures 3-5). The two models exhibit differing behaviour during the night: the Schuster model exhibits ongoing weathering crust growth, albeit at a reduced rate compared to the growth phase; whilst the Woods model exhibits a top-down density increase.

5.2 Exploration of model performance

5.2.1 Individual core segment density prediction

One explanation for the difference between modelled and field density is that modelled energy distribution across the depth profile poorly reflects the real-world weathering process. This process is represented in the models by the extinction coefficient, which defines the absorption, scattering, and therefore energy flux from SWR through the ice column. The Schuster model uses an extinction coefficient of 6 m^{-1}, and the Woods model a combined scattering and absorption coefficient which sums an extinction coefficient to 4.4 m^{-1}. One potential avenue to improve the alignment between the model output and field data is to us a different extinction coefficient. However, we do not attempt to tune a single constant value for this poorly understood variable, especially without a physical dataset to do so. The use of a single broadband extinction coefficient may not be appropriate due to the way glacier ice absorbs and scatters light, and the dynamic nature of an actively evolving weathering crust. Several studies (Cooper and others 2021; Warren 1984; Warren and others 2006) highlight the wavelength-variable absorption and transmission of light through glacier ice, implying differential maximum penetration depths for light of different wavelengths. Furthermore, the specific surface area (SSA) of the ice (a measure capturing the surface of scattering interfaces per unit mass) changes as the weathering crust evolves, implying that the extinction coefficient also changes temporally. One future avenue to establish such a dynamic extinction coefficient, that corresponds more closely to real world conditions, would be to couple a weathering crust evolution model with a radiative transfer model that calculates depth-variable extinction coefficients accounting for spatiotemporally variable SSA.

The Woods model appears to underestimate ice melt rates and overestimates the role of meltwater refreezing than is observed in the field, resulting in overestimation of ice density. As meltwater is not considered in the Schuster model (Table 1), the following analysis is relevant only to the Woods model. In addition to consideration of the extinction coefficient, the Woods model also requires further hydrological development to reach its full potential. For example, such development could include the addition of an active water table, which is observed in the weathering crust (Cook and others, 2015; Stevens and others 2018). This goal could be achieved using estimates of weathering crust hydraulic conductivity and throughflow (Doting and others 2025; Irvine-Fynn and others 2021; Stevens and others 2018) to prescribe drainage values, or by building empirical relationships between ice density and critical hydrological variables such as effective porosity (e.g. Cooper and others 2018; Halbach and others 2023). Such development would lessen the refreeze-effect, and more accurately resemble the real-world setting where the water table in the weathering crust is > 0.1 m below the surface (e.g. Stevens et al. 2018).

5.2.2 Replication of the growth-decay-growth evolution pattern

The Schuster model does not replicate the decay phase observed in the field data. The model functions by calculating the relative rates of surface lowering with internal mass loss, by partitioning energy across the depth profile (Table 1), and weathering crust decay occurs when the rate of surface lowering exceeds the rate of internal mass loss. To reproduce weathering crust decay, the Schuster model requires high turbulent energy flux and low SWR flux, but these conditions do not appear to occur in our meteorological measurement window. The model's lack of capability to consider meltwater refreezing appears to limit its ability to reproduce the observed decay phase.

In contrast, the Woods model demonstrates substantial density gain during the decay phase, through the process of meltwater refreezing. Unsurprisingly, this process is more prevalent with lower air temperatures: the refreeze front depth only reaches 0.02 m depth for S15, whilst it reaches 0.12 m and 0.16 m for WCRs 1 & 2 and 3 & 4, respectively (Figure 5). Observation periods with colder air temperatures (Figure 2) enable the frozen front to penetrate deeper within the ice column. This is exemplified by our data: for S15 the freeze front penetrates the weathering crust for < 2 hours; WCRs 1 & 2 for ~8.5 hours; and almost 14 hours for WCRs 3 & 4. The onset of this freezing period occurs around midnight in all model runs, two hours after SWR receipt is reduced to ~0 W m^{-2} (at ~2200, Figure 2). In the regrowth phase, the rate of weathering accelerates (c.f. the overnight reduction in weathering rate) for the Schuster model. In the Woods model, the frozen front persists for the length of the model run, generating a stepped, partially inverted density profile (Figure 5), not observed in the field observations (Figure 3).

The differing behaviour of the two models during the decay phase can be explained by the assumptions each model is based upon, as summarised in Table 1. When considered alongside the field data, such behaviour further reinforces the assertion that density increase in the decay phase is driven by multiple processes. The Schuster model assumes that ice is at the melting point (it has no explicit ice temperature simulation), and that the interstitial pore space is occupied by air – as such it cannot simulate refreezing. It fails to reproduce the observed densification of the weathering crust, further supporting the argument that surface lowering alone does not drive weathering crust decay. In contrast, the Woods model explicitly models ice temperature and assumes that the pore space is occupied by meltwater. As such, the Woods model is capable of simulating density increase in conditions of negative surface energy balance, through the process of refreezing interstitial meltwater. However, the simulated behaviour does not correspond with the field observations of ice density, further supporting the argument that refrozen meltwater accretion is not a significant driver of density increase during the overnight weathering crust decay phase. It should be noted that neither model simulates hoar frost deposition.

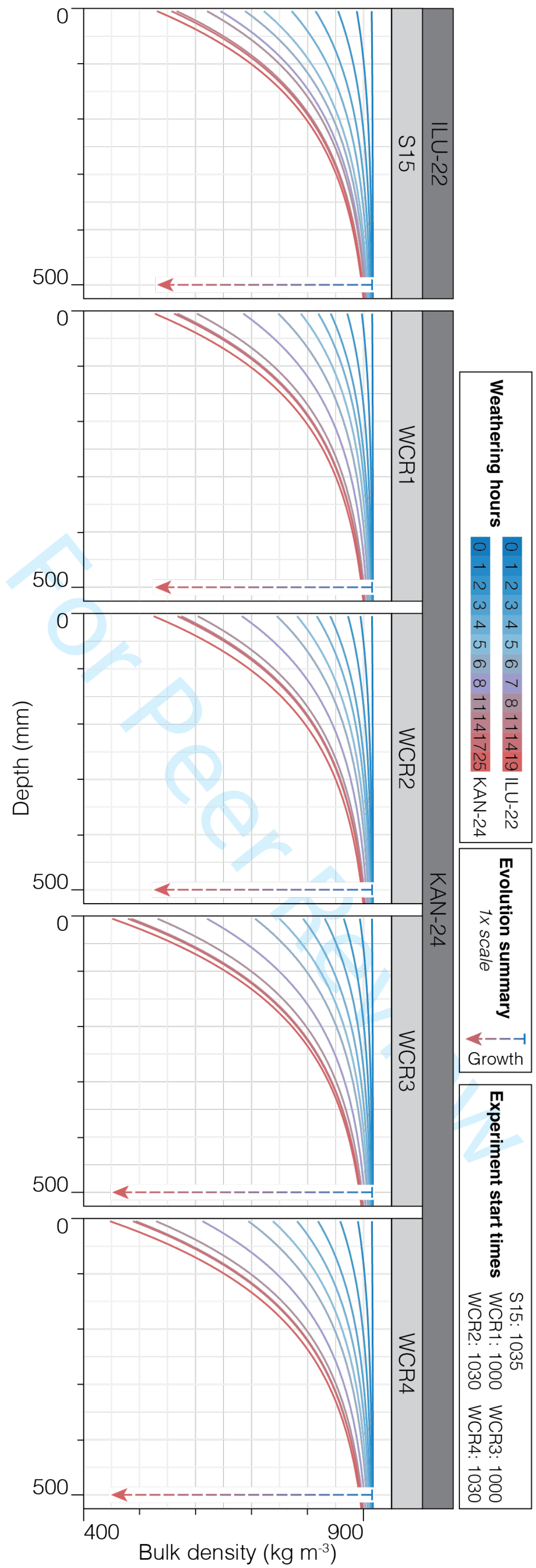

Figure 4 | Modelled weathering crust reset experiments, using the Schuster (2001) model, showing change in ice density (y axis) across the depth profile (x axis), over time (line colour). Timesteps correspond with those of Figure 3 (field measured depth-density). This model does not how three-phase evolution, only a growth phase. Each observation period is given one row.

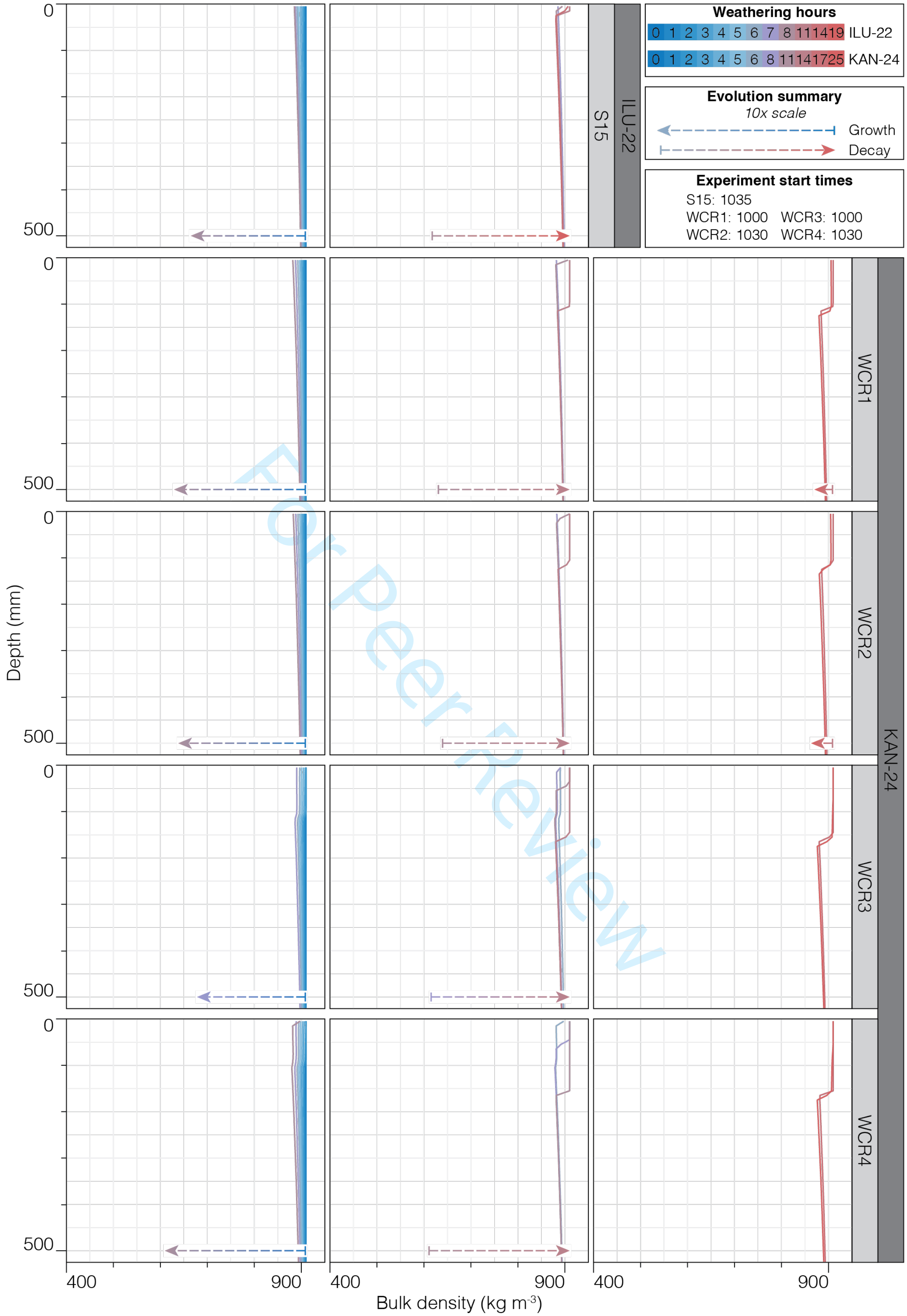

Figure 5 | Modelled weathering crust reset experiments, using the Woods (2023, 2024) model, showing change in ice density (y axis) across the depth profile (x axis), over time (line colour). Timesteps correspond with those of Figure 3 (field measured depth-density), as does the three-phase evolution pattern. Note the scale of the 'evolution summary' arrow. Each observation period is given one row.

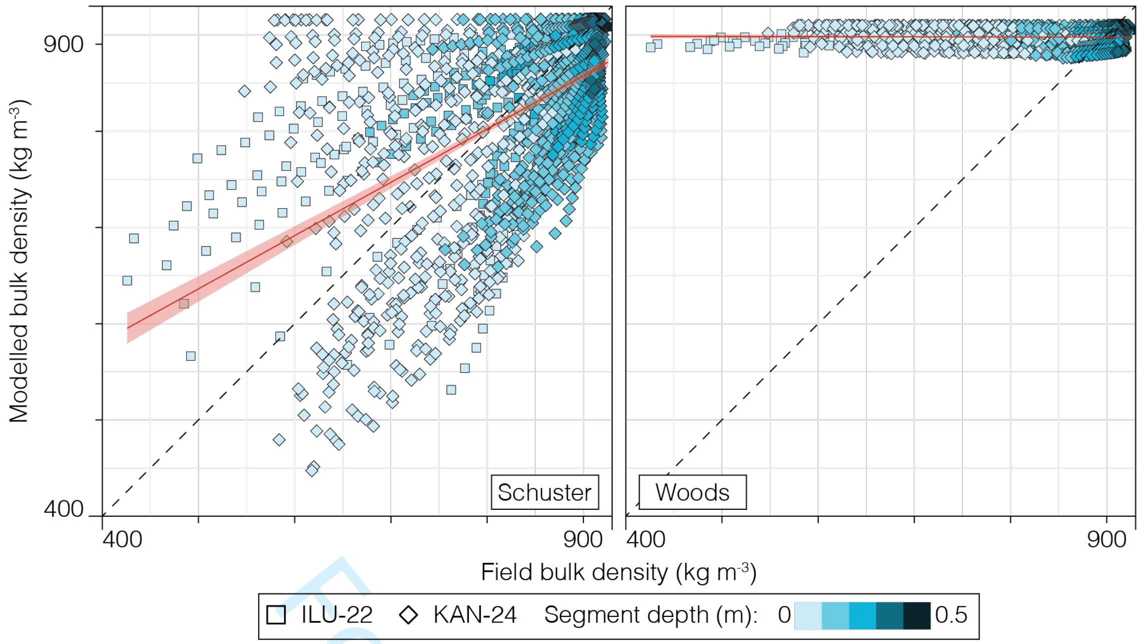

Figure 6 | Modelled bulk ice density *cf.* field measured bulk density for each of the two models. The dashed line indicates a 'perfect density estimate' (i.e., field measured density equal to modelled density). Segment depth (0.1 m bins) is indicated using colour, whilst core location is indicated by point shape. There is no systemic relationship between under/over prediction of density and core segment depth or field site. A linear model fit is presented in red, to assist with the comparative visualisation of the data to the dashed line of 1:1 modelled-field density ratio.

6. The contribution of ice weathering to broadband albedo

Broadband albedo was measured prior to core abstraction at each site between the hours of 1000 – 1800 (i.e. solar noon ± ~5 hours), generating 48 individual measurements of broadband albedo from our experimental surfaces. We report different broadband bare ice albedo at each of our study locations: for ILU-22 we report albedos between 0.52 and 0.58, and for KAN-24 we report much lower albedos between 0.38 and 0.45. Both ranges correspond with the reference values for 'clean-ice' albedo (Cuffey and Paterson 2010), and our ILU-22 albedos fall within observed range for clean ice on the Greenland Ice Sheet (Wehrlé and others 2021). We attribute the difference in albedo between the two sites to two causes: the use of different instrumentation, and the possibility of greater particulate loading at KAN-24 than at ILU-22. For the ILU-22 campaign (the S15 experiment), surface reflectance was measured over a well-defined footprint, using a 10° field of view. In contrast, albedo was measured using a semi-hemispheric Kipp and Zonen CNR4 at KAN-24 (150° field of view), potentially incorporating interference from non-ice reflectors. Furthermore, despite cleaning of the experimental surface, it was not possible to remove particulates from within the ice column – despite the underlying assumption that it was 'clean' – and it is probably that this inherent 'darkness' also causes lower albedo observations for the KAN-24 sites; especially as the area around the S6 weather station is renowned for its typically lower-than-average albedo (e.g. Feng and others 2023; Greuell 2000; van den Broeke and others 2008).

Our data reveal that bulk ice density of the uppermost 0.1 m of the weathering crust exerts a strong control on bare ice albedo (Figure 8). The average ice density of this upper section of the weathering crust describes 88 to 96% of the variation in bare ice broadband albedo throughout our experiment – which we caution was undertaken on an LAP-free, modified surface, rather than a surface in its natural state. This is further supported by the variations in spectral albedo, which primarily occurred in the near-infrared region (Supplementary Figure 7) where the physical properties of ice are the main control on albedo (Gardner and Sharp 2010; Whicker and others 2022). We attribute the governing role of near-surface ice density over broadband bare ice albedo to structural changes in the ice crystal matrix associated with weathering, which increases internal scattering. Ice is poorly absorbing in the spectral domain corresponding to SWR (Warren 2019) and consequently the extinction of light within and from the ice column is primarily controlled by the amount of scattering. Scattering is primarily governed by the SSA of polycrystalline ice (Gardner and Sharp 2010), which describes the per-mass surface of air-ice interface area (i.e., the surface area of ice crystals in a given mass of ice) where scattering events occur. SSA is governed by effective grain and pore (also referred to 'bubble') size. A dense ice column with few large bubbles has a low SSA and high SWR penetration depth, while a porous column with small air inclusions has a high SSA. The formation of the weathering crust is, to a degree, a negative-feedback process, in which weathering increases porosity and consequently SSA, causing more scattering, increasing broadband surface albedo and reducing depth penetration of SWR. This feedback is further complicated by the presence of water within the weathering crust, which can fill pore spaces and reduce SSA, scatter, and albedo. The uppermost 0.1 m of the weathering crust (as examined in this analysis) is generally unsaturated (Cook and others 2015; Stevens and others 2018), containing only crystal-bound meltwater. Hence, the role of water is not relevant to the analysis herein – but the role of interstitial meltwater cannot be disregarded in the rare cases where the water table is within 0.1 m of the ice surface.

For the range of ice densities measured herein, our data demonstrate that ice condition can drive a maximum albedo change of 0.05. However, it is unclear whether our experimental surfaces reach equilibrium with a fully developed weathering crust (discussed in further detail in section 4), and as such this value is unlikely to represent the fully range of density-controlled albedo. By extrapolating the linear relationships identified in Figure 7, using the lowest quoted value for weathering crust density for the uppermost 0.1 m (300 kg m^{-3}; Cooper and others 2018; LaChapelle 1959) we imply that near surface ice density has the potential to increase albedo by 0.09 *cf.* unweathered ice. Despite the strong governing relationship of near-surface ice density on bare ice albedo, the contribution of weathering crust condition to overall albedo can be considered secondary to the admixture of light absorbing impurities found on the ice surface (e.g. Chevrollier and others 2022; Cook and others 2020; Ryan and others 2018; Williamson and others 2020). Previous work has reported that surface algae can directly reduce albedo by up to 0.10 (Chevrollier and others 2022), and that the presence of 'biologically active impurities' (e.g. algae and dispersed cryoconite material) can drive an albedo reduction of ~0.2 when contrasted with 'clean' ice (after Ryan and others 2018). Ultimately, the physical condition of near-surface ice plays a role in defining broadband surface albedo, but its relative contribution is lower than that of LAPs at a point scale.

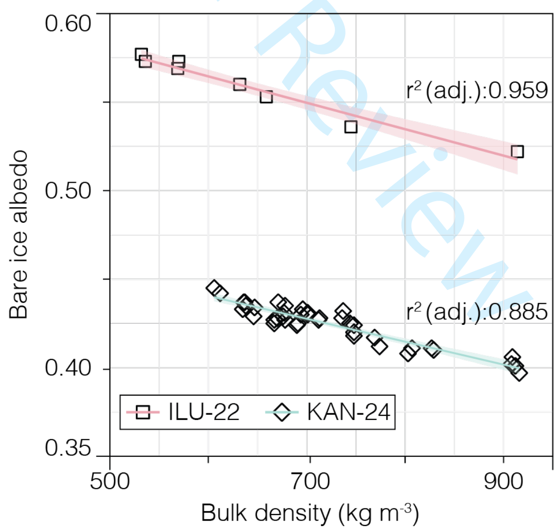

Figure 7 | Bare ice albedo as a function of bulk density of the uppermost 0.1 m of the ice column. Shape and colour are used to differentiate field locations. Adjusted r^2 is presented per location to describe the linear model fit, within the measurement bounds.

7. Summary

We present a method to 'reset' the near-surface weathering crust and measure its development, well suited to explorations of its evolution. Our 383 measurements on the Greenland Ice Sheet reveal ice densities from 420 kg m^{-3} to 920 kg m^{-3}, providing the largest study of weathering crust condition to date. We observe the hypothesised non-linear depth-density relationship, a result of the non-linear receipt of SWR throughout the ice column. However, we typically observe shallower weathering crusts than previous work has suggested: we report depths of up to 0.5 m, whilst others report depths up to 2 m.

We reveal diurnal switching behaviour in the process of weathering crust evolution. During the day, under clear sky conditions (i.e. high SWR receipt), the near-surface of the ice is actively – and potentially rapidly – weathering. An unweathered ice surface evolves quickly, with the uppermost ~0.05 m of the ice column weathering at rates of up to -80 kg m^{-3} hr^{-1}. During periods of low SWR receipt (in this case, overnight – but this could also occur under cloudy conditions) weathering rate reduces, and the density of the weathering crust effectively increases. We suggest that a combination of surface lowering, refreezing of interstitial meltwater, and hoar deposition drive this process. Density reduction resumes following a return to 'high' SWR conditions. This rapid rate of change of near-surface ice density has implications for supraglacial hydrology: the weathering crust demonstrates the potential to change on an hourly timescale, which will affect its effective porosity and meltwater transmissivity. Ice density in the upper 0.1 m of the ice column demonstrates a negative relationship with bare ice albedo: weathered ice is more reflective than unweathered ice. The magnitude of this effect is important, but it is secondary to the competing role of light absorbing particles (LAPs).

Two numerical models describing weathering crust formation (Schuster 2001; Woods and Hewitt 2023; 2024) were evaluated against our field measurements. Neither model reliably recreates the field observations. The Woods model produced thin weathering crusts with high densities (< 0.1 m deep and minimum densities > 880 kg m^{-3}), while the Schuster model failed to capture the overnight decay phase of the weathering crust, and underestimated weathering when field measurements of ice density are less than 800 kg m^{-3}. Ultimately, this reveals that we still have a poor mechanistic understanding of near-surface ice weathering, most notably the partitioning of energy between the ice surface and near-surface, and the absorption/extinction/reflection of light through a column of polycrystalline ice.

Acknowledgements

This work was funded by the ERC-Synergy grant 'Deep Purple' (Grant agreement ID: 856416) to AMA, LGB, and MT, and the Rolex Awards for Enterprise to JMC. ITS acknowledges support from the Program for Monitoring the Greenland Ice Sheet (PROMICE), and AJH acknowledges support from Aberystwyth University's 150th Anniversary Fellowship Scheme. The authors would like to thank Paul Smeets (Institute for Marine and Atmospheric Research, Utrecht University) for providing meteorological data for S6 for the summer of 2024; Tilly Woods, Ian Hewitt and Corinne Schuster for their work developing the models implemented herein; and Andrew Tedstone for translating the Brock and Arnold (2000) implementation of the bulk-aerodynamic method into Python.

Author Contributions

ITS conceived the concept of this study, designed the study approach, collected field data (2022 and 2024), contributed to model development, testing, and model runs (both Schuster and Woods), analysed the data, produced the figures, and wrote the paper. JMC translated and tested the Schuster model and contributed to data analysis. L-AC contributed to the design of the study approach, measured spectral reflectance in the field (2022), and processed the spectral data. AJH added measured forcing to the Woods model, ran the model, and contributed to the model data analysis. AMA measured broadband albedo in the field (2024), and alongside LGB and MT, funded this work. All authors contributed to editing and revision of the manuscript. Generative AI was not used in any element of this research.

Data and Code Availability

All data, model code, and code required to reproduce (rudimentary) copies of each figure element (exc. Figure 1) can be found at [*to be uploaded*].

Competing Interests

The authors report no competing interests.

Reference List

Arnold NS, Rees WG, Hodson AJ and Kohler J (2006) Topographic controls on the surface energy balance of a high Arctic valley glacier. *Journal of Geophysical Research: Earth Surface* **111**(F2). https://doi.org/https://doi.org/10.1029/2005JF000426.

Beer A (1852) Bestimmung der Absorption des rothen Lichts in farbigen Flüssigkeiten. *Annalen der Physik* **162**(5)**,** 78-88.

Braithwaite RJ (2009) Calculation of sensible-heat flux over a melting ice surface using simple climate data and daily measurements of ablation. *Annals of Glaciology* **50**(50)**,** 9-15. https://doi.org/10.3189/172756409787769726.

Brock BW and Arnold NS (2000) A spreadsheet-based (Microsoft Excel) point surface energy-balance model for glacier and snow melt studies. *Earth Surface Processes and Landforms* **25,** 649-658.

Brock BW, Mihalcea C, Kirkbride MP, Diolaiuti G, Cutler MEJ and Smiraglia C (2010) Meteorology and surface energy fluxes in the 2005–2007 ablation seasons at the Miage debris-covered glacier, Mont Blanc Massif, Italian Alps. *Journal of Geophysical Research: Atmospheres* **115**(D9). https://doi.org/doi:10.1029/2009JD013224.

Cameron KA, Hodson AJ and Osborn AM (2012) Carbon and nitrogen biogeochemical cycling potentials of supraglacial cryoconite communities. *Polar Biology* **35**(9)**,** 1375-1393. https://doi.org/10.1007/s00300-012-1178-3.

Chevrollier L-A, Cook JM, Halbach L, Jakobsen H, Benning LG, Anesio AM and Tranter M (2022) Light absorption and albedo reduction by pigmented microalgae on snow and ice. *Journal of Glaciology***,** 1-9. https://doi.org/10.1017/jog.2022.64.

Chu VW (2014) Greenland ice sheet hydrology:A review. *Progress in Physical Geography: Earth and Environment* **38**(1)**,** 19-54. https://doi.org/10.1177/0309133313507075.

Cook J, Edwards A, Takeuchi N and Irvine-Fynn T (2016) Cryoconite:The dark biological secret of the cryosphere. *Progress in Physical Geography: Earth and Environment* **40**(1)**,** 66-111. https://doi.org/10.1177/0309133315616574.

Cook JM, Hodson AJ and Irvine-Fynn TDL (2015) Supraglacial weathering crust dynamics inferred from cryoconite hole hydrology. *Hydrological Processes***,** n/a-n/a. https://doi.org/10.1002/hyp.10602.

Cook JM, Tedstone AJ, Williamson C, McCutcheon J, Hodson AJ, Dayal A, Skiles M, Hofer S, Bryant R, McAree O, McGonigle A, Ryan J, Anesio AM, Irvine-Fynn TDL, Hubbard A, Hanna E, Flanner M, Mayanna S, Benning LG, van As D, Yallop M, McQuaid JB, Gribbin T and Tranter M (2020) Glacier algae accelerate melt rates on the south-western Greenland Ice Sheet. *The Cryosphere* **14**(1)**,** 309-330. https://doi.org/10.5194/tc-14-309-2020.

Cooper MG, Smith LC, Rennermalm AK, Miège C, Pitcher LH, Ryan JC, Yang K and Cooley SW (2018) Meltwater storage in low-density near-surface bare ice in the Greenland ice sheet ablation zone. *The Cryosphere* **12**(3)**,** 955-970. https://doi.org/10.5194/tc-12-955-2018.

Cooper MG, Smith LC, Rennermalm AK, Tedesco M, Muthyala R, Leidman SZ, Moustafa SE and Fayne JV (2021) Spectral attenuation coefficients from measurements of light transmission in bare ice on the Greenland Ice Sheet. *The Cryosphere* **15**(4)**,** 1931-1953. https://doi.org/10.5194/tc-15-1931-2021.

Cuffey KM and Paterson WSB (2010) *The Physics of Glaciers*, 4th edn. London: Butterworth-Heinemann.

Derikx L (1973) Glacier discharge simulation by groundwater analogue. In: *Hydrology of Glaciers.* Cambridge: IAHS.

Doting EL, Stevens IT, Kellerman AM, Rossel PE, Antony R, McKenna AM, Tranter M, Benning LG, Spencer RGM, Hawkings JR and Anesio AM (2025) Molecular-level characterization of supraglacial dissolved and water-extractable organic matter along a hydrological flow path in a Greenland Ice Sheet micro-catchment. *Biogeosciences* **22**(1)**,** 41-53. https://doi.org/10.5194/bg-22-41-2025.

Edwards A, Irvine-Fynn TDL, Mitchell AC and Rassner SME (2014) A germ theory for glacial systems? *WIREs: Water* **1,** 331-340. https://doi.org/10.1002/wat2.1029.

Faber Q, Davis C and Christner B (2024) Metagenomic inference of microbial community composition and function in the weathering crust aquifer of a temperate glacier. *Frontiers in Microbiomes* **3**. https://doi.org/10.3389/frmbi.2024.1488744.

Fausto RS, van As D, Mankoff KD, Vandecrux B, Citterio M, Ahlstrøm AP, Andersen SB, Colgan W, Karlsson NB, Kjeldsen KK, Korsgaard NJ, Larsen SH, Nielsen S, Pedersen AØ, Shields CL, Solgaard AM and Box JE (2021) Programme for Monitoring of the Greenland Ice Sheet (PROMICE) automatic weather station data. *Earth Syst. Sci. Data* **13**(8)**,** 3819-3845. https://doi.org/10.5194/essd-13-3819-2021.

Feng S, Cook JM, Anesio AM, Benning LG and Tranter M (2023) Long time series (1984–2020) of albedo variations on the Greenland ice sheet from harmonized Landsat and Sentinel 2 imagery. *Journal of Glaciology***,** 1-16. https://doi.org/10.1017/jog.2023.11.

Fettweis X, Franco B, Tedesco M, van Angelen JH, Lenaerts JTM, van den Broeke MR and Gallée H (2013) Estimating the Greenland ice sheet surface mass balance contribution to future sea level rise using the regional atmospheric climate model MAR. *The Cryosphere* **7**(2), 469-489. https://doi.org/10.5194/tc-7-469-2013.

Fierz C, Armstrong RL, Durand Y, Etchevers P, Greene E, McClung DM, Nishimura K, Satyawali PK and Sokratov SA (2009) The international classification for seasonal snow on the ground.

Fountain AG and Walder JS (1998) Water flow through temperate glaciers. *Reviews of Geophysics* **36**(3), 299-328.

Gantayat P, Banwell AF, Leeson AA, Lea JM, Petersen D, Gourmelen N and Fettweis X (2023) A new model for supraglacial hydrology evolution and drainage for the Greenland Ice Sheet (SHED v1.0). *Geosci. Model Dev.* **16**(20), 5803-5823. https://doi.org/10.5194/gmd-16-5803-2023.

Gardner AS and Sharp MJ (2010) A review of snow and ice albedo and the development of a new physically based broadband albedo parameterization. *Journal of Geophysical Research: Earth Surface* **115**(F1). https://doi.org/10.1029/2009JF001444.

Geiger R (1965) *Das Klima Der Bodennahen Luftschicht. The Climate Near the Ground. Translated from the 4th German Ed. by Scripta Technica, Inc*. Harvard University Press.

Gleason CJ, Yang K, Feng D, Smith LC, Liu K, Pitcher LH, Chu VW, Cooper MG, Overstreet BT, Rennermalm AK and Ryan JC (2021) Hourly surface meltwater routing for a Greenlandic supraglacial catchment across hillslopes and through a dense topological channel network. *The Cryosphere* **15**(5), 2315-2331. https://doi.org/10.5194/tc-15-2315-2021.

Grenfell TC and Maykut GA (1977) The Optical Properties of Ice and Snow in the Arctic Basin. *Journal of Glaciology* **18**(80), 445-463. https://doi.org/10.3189/S0022143000021122.

Grenfell TC and Perovich DK (1981) Radiation absorption coefficients of polycrystalline ice from 400–1400 nm. *Journal of Geophysical Research: Oceans* **86**(C8), 7447-7450. https://doi.org/https://doi.org/10.1029/JC086iC08p07447.

Greuell W (2000) Melt–water accumulation on the surface of the Greenland ice sheet: Effect on albedo and mass balance. *Geografiska Annaler: Series A, Physical Geography* **82**(4), 489-498.

Greuell W and Oerlemans J (1989) The evolution of the englacial temperature distribution in the superimposed ice zone of a polar ice cap during a summer season. In Oerlemans J (ed), *Glacier Fluctuations and Climatic Change: Proceedings of the Symposium on Glacier Fluctuations and Climatic Change, held in Amsterdam, 1–5 June 1987.* Dordrecht: Springer Netherlands, 289-303.

Halbach L, Chevrollier L-A, Cook JM, Stevens IT, Hansen M, Anesio AM, Benning LG and Tranter M (2023) Dark ice in a warming world: advances and challenges in the study of Greenland Ice Sheet's biological darkening. *Annals of Glaciology*, 1-6. https://doi.org/10.1017/aog.2023.17.

Hock R (2005) Reveiw of melt processes. *Progress in Physical Geography* **29**(3), 362-391.

Hoffman MJ, Fountain AG and Liston GE (2014) Near-surface internal melting: a substantial mass loss on Antarctic Dry Valley glaciers. *Journal of Glaciology* **60**(220), 361-374. https://doi.org/10.3189/2014JoG13J095.

Horton S, Schirmer M and Jamieson B (2015) Meteorological, elevation, and slope effects on surface hoar formation. *The Cryosphere* **9**(4), 1523-1533. https://doi.org/10.5194/tc-9-1523-2015.

Hugonnet R, McNabb R, Berthier E, Menounos B, Nuth C, Girod L, Farinotti D, Huss M, Dussaillant I, Brun F and Kääb A (2021) Accelerated global glacier mass loss in the early twenty-first century. *Nature* **592**(7856), 726-731. https://doi.org/10.1038/s41586-021-03436-z.

Huss M and Hock R (2018) Global-scale hydrological response to future glacier mass loss. *Nature Climate Change* **8**(2), 135-140. https://doi.org/10.1038/s41558-017-0049-x.

Irvine-Fynn TDL and Edwards A (2014) A frozen asset: the potential of flow cytometry in constraining the glacial biome. *Cytometry A* **85**(1), 3-7. https://doi.org/10.1002/cyto.a.22411.

Irvine-Fynn TDL, Edwards A, Stevens IT, Mitchell AC, Bunting P, Box JE, Cameron KA, Cook JM, Naegeli K, Rassner SME, Ryan JC, Stibal M, Williamson CJ and Hubbard A (2021) Storage and export of microbial biomass across the western Greenland Ice Sheet. *Nature Communications* **12**(1), 3960. https://doi.org/10.1038/s41467-021-24040-9.

Jennings SJA and Hambrey MJ (2021) Structures and Deformation in Glaciers and Ice Sheets. *Reviews of Geophysics* **59**(3), e2021RG000743. https://doi.org/https://doi.org/10.1029/2021RG000743.

Koizumi K and Naruse R (1994) Experiments on formation of water channels in a glacier. *Journal of the Japanese Society of Snow and Ice* **56**(2), 137-144. https://doi.org/10.5331/seppyo.56.137.

LaChapelle E (1959) Errors in ablation measurements from settlement and sub-surface melting. *Journal of Glaciology* **3**(26), 458-467.

Larson GJ (1977) Internal drainage of stagnant ice: Burroughs Glacier, southeast Alaska. Institute of Polar Studies, Ohio State University.

Larson GJ (1978) Meltwater storage in a temperate glacier: Burroughs Glacier, Southeast Alaska. Institute of Polar Studies, Ohio State University.

Litt M, Sicart JE, Six D, Wagnon P and Helgason WD (2017) Surface-layer turbulence, energy balance and links to atmospheric circulations over a mountain glacier in the French Alps. *The Cryosphere* **11**(2), 971-987. https://doi.org/10.5194/tc-11-971-2017.

Mader HM (1992) Observations of the Water-Vein System in Polycrystalline Ice. *Journal of Glaciology* **38**(130), 333-347.

Maturilli M (2020) Continuous meteorological observations at station Ny-Ålesund (2011-08 et seq). In.: PANGAEA.

Mayerhöfer TG, Pahlow S and Popp J (2020) The Bouguer-Beer-Lambert Law: Shining Light on the Obscure. *Chemphyschem* **21**(18), 2029-2046. https://doi.org/10.1002/cphc.202000464.

McCutcheon J, Lutz S, Williamson C, Cook JM, Tedstone AJ, Vanderstraeten A, Wilson SA, Stockdale A, Bonneville S, Anesio AM, Yallop ML, McQuaid JB, Tranter M and Benning LG (2021) Mineral phosphorus drives glacier algal blooms on the Greenland Ice Sheet. *Nature Communications* **12**(1), 570. https://doi.org/10.1038/s41467-020-20627-w.

Müller F and Keeler CM (1969) Errors in short term ablation measurement on melting ice surfaces. *Journal of Glaciology* **8**(52), 91-105.

Munro DS (1990) Comparison of Melt Energy Computations and Ablatometer Measurements on Melting Ice and Snow. *Arctic and Alpine Research* **22**(2), 153-162. https://doi.org/Doi 10.2307/1551300.

Munro DS (2011) Delays of supraglacial runoff from differently defined microbasin areas on the Peyto Glacier. *Hydrological Processes*, 2983-2994. https://doi.org/10.1002/hyp.8124.

Noël B, van Kampenhout L, Lenaerts JTM, van de Berg WJ and van den Broeke MR (2021) A 21st Century Warming Threshold for Sustained Greenland Ice Sheet Mass Loss. *Geophysical Research Letters* **48**(5), e2020GL090471. https://doi.org/https://doi.org/10.1029/2020GL090471.

Nye F and Frank FC (1973) Hydrology of the intergranular veins in a temperate glacier. In: *Hydrology of Glaciers.* Cambridge: IAHS.

Nye JF (1991) The rotting of temperate ice. *Journal of Crystal Growth* **113**(3–4), 465-476. https://doi.org/http://dx.doi.org/10.1016/0022-0248(91)90081-F.

Ohmura A and Boettcher M (2022) On the Shift of Glacier Equilibrium Line Altitude (ELA) under the Changing Climate. *Water* **14**(18), 2821.

Oke TR (1987) *Boundary Layer Climates*. London: Routledge.

Pitcher LH and Smith LC (2019) Supraglacial Streams and Rivers. *Annual Review of Earth and Planetary Sciences* **47**(1), 421-452. https://doi.org/10.1146/annurev-earth-053018-060212.

Rassner SME, Cook JM, Mitchell AC, Stevens IT, Irvine-Fynn TDL, Hodson AJ and Edwards A (2024) The distinctive weathering crust habitat of a High Arctic glacier comprises discrete microbial micro-habitats. *Environmental Microbiology* **26**(4), e16617. https://doi.org/https://doi.org/10.1111/1462-2920.16617.

Rounce DR, Hock R, Maussion F, Hugonnet R, Kochtitzky W, Huss M, Berthier E, Brinkerhoff D, Compagno L, Copland L, Farinotti D, Menounos B and McNabb RW (2023) Global glacier change in the 21st century: Every increase in temperature matters. *Science* **379**(6627), 78-83. https://doi.org/doi:10.1126/science.abo1324.

Ryan JC, Hubbard A, Stibal M, Irvine-Fynn TD, Cook J, Smith LC, Cameron K and Box J (2018) Dark zone of the Greenland Ice Sheet controlled by distributed biologically-active impurities. *Nature Communications* **9**(1), 1065. https://doi.org/10.1038/s41467-018-03353-2.

Schuster CJ (2001) Weathering crust processes on melting glacier ices (Alberta, Canada). PhD, Wilfred Laurier University.

Smeets PCJP, Kuipers Munneke P, van As D, van den Broeke MR, Boot W, Oerlemans H, Snellen H, Reijmer CH and van de Wal RSW (2018) The K-transect in west Greenland: Automatic weather station data (1993–2016). *Arctic, Antarctic, and Alpine Research* **50**(1), S100002. https://doi.org/10.1080/15230430.2017.1420954.

Smith LC, Chu VW, Yang K, Gleason CJ, Pitcher LH, Rennermalm AK, Legleiter CJ, Behar AE, Overstreet BT, Moustafa SE, Tedesco M, Forster RR, LeWinter AL, Finnegan DC, Sheng Y and Balog J (2015) Efficient meltwater drainage through supraglacial streams and rivers on the southwest Greenland ice sheet. *Proceedings of the National Academy of Sciences* **112**(4), 1001-1006. https://doi.org/10.1073/pnas.1413024112.

Smith LC, Yang K, Pitcher LH, Overstreet BT, Chu VW, Rennermalm ÅK, Ryan JC, Cooper MG, Gleason CJ, Tedesco M, Jeyaratnam J, van As D, van den Broeke MR, van de Berg WJ, Noël B, Langen PL, Cullather RI, Zhao B, Willis MJ, Hubbard A, Box JE, Jenner BA and Behar AE (2017) Direct measurements of meltwater runoff on the Greenland ice sheet surface. *Proceedings of the National Academy of Sciences* **114**(50), E10622-E10631. https://doi.org/10.1073/pnas.1707743114.

Stevens IT (2019) The Eco-Hydrology of Glacier Surfaces. PhD, Geography and Earth Sciences, Aberystwyth University.

Stevens IT, Irvine-Fynn TDL, Edwards A, Mitchell AC, Cook JM, Porter PR, Holt TO, Huss M, Fettweis X, Moorman BJ, Sattler B and Hodson AJ (2022) Spatially consistent microbial biomass and future cellular carbon release from melting Northern Hemisphere glacier surfaces. *Communications Earth & Environment* **3**(1), 275. https://doi.org/10.1038/s43247-022-00609-0.

Stevens IT, Irvine-Fynn TDL, Porter PR, Cook JM, Edwards A, Smart M, Moorman BJ, Hodson AJ and Mitchell AC (2018) Near-surface hydraulic conductivity of northern hemisphere glaciers. *Hydrological Processes* **32**(7), 850-865. https://doi.org/doi:10.1002/hyp.11439.

Takeuchi N (2009) Temporal and spatial variations in spectral reflectance and characteristics of surface dust on Gulkana Glacier, Alaska Range. *Journal of Glaciology* **55**(192), 701-709.

Tedstone AJ, Cook JM, Williamson CJ, Hofer S, McCutcheon J, Irvine-Fynn T, Gribbin T and Tranter M (2020) Algal growth and weathering crust state drive variability in western Greenland Ice Sheet ice albedo. *The Cryosphere* **14**(2), 521-538. https://doi.org/10.5194/tc-14-521-2020.

van den Broeke M, Smeets P, Ettema J and Munneke PK (2008) Surface radiation balance in the ablation zone of the west Greenland ice sheet. *Journal of Geophysical Research: Atmospheres* **113**(D13). https://doi.org/https://doi.org/10.1029/2007JD009283.

van Tiggelen M, Smeets PCJP, Reijmer CH, van As D, Box JE, Fausto RS, Khan SA, Rignot E and van den Broeke MR (2024) Surface energy balance closure over melting snow and ice from in situ measurements on the Greenland ice sheet. *Journal of Glaciology*, 1-11. https://doi.org/10.1017/jog.2024.68.

Warren SG (1984) Optical constants of ice from the ultraviolet to the microwave. *Applied Optics* **23**(8), 1206-1225. https://doi.org/10.1364/AO.23.001206.

Warren SG (2019) Optical properties of ice and snow. *Philosophical Transactions of the Royal Society A* **377**(2146), 20180161.

Warren SG, Brandt RE and Grenfell TC (2006) Visible and near-ultraviolet absorption spectrum of ice from transmission of solar radiation into snow. *Applied Optics* **45**(21), 5320-5334. https://doi.org/10.1364/AO.45.005320.

Wehrlé A, Box JE, Niwano M, Anesio AM and Fausto RS (2021) Greenland bare-ice albedo from PROMICE automatic weather station measurements and Sentinel-3 satellite observations. *GEUS Bulletin* **47**. https://doi.org/10.34194/geusb.v47.5284.

Whicker CA, Flanner MG, Dang C, Zender CS, Cook JM and Gardner AS (2022) SNICAR-ADv4: a physically based radiative transfer model to represent the spectral albedo of glacier ice. *The Cryosphere* **16**(4), 1197-1220. https://doi.org/10.5194/tc-16-1197-2022.

Wientjes IGM, Van de Wal RSW, Reichart GJ, Sluijs A and Oerlemans J (2011) Dust from the dark region in the western ablation zone of the Greenland ice sheet. *Cryosphere* **5**(3), 589-601. https://doi.org/DOI 10.5194/tc-5-589-2011.

Wientjes IGM, Van De Wal RSW, Schwikowski M, Zapf A, Fahrni S and Wacker L (2012) Carbonaceous particles reveal that Late Holocene dust causes the dark region in the western ablation zone of the Greenland ice sheet. *Journal of Glaciology* **58**(210), 787-794. https://doi.org/10.3189/2012JoG11J165.

Williamson CJ, Cook J, Tedstone A, Yallop M, McCutcheon J, Poniecka E, Campbell D, Irvine-Fynn T, McQuaid J, Tranter M, Perkins R and Anesio A (2020) Algal photophysiology drives darkening and melt of the Greenland Ice Sheet. *Proceedings of the National Academy of Sciences* **117**(11), 5694-5705. https://doi.org/10.1073/pnas.1918412117.

Woods T and Hewitt IJ (2023) A model of the weathering crust and microbial activity on an ice-sheet surface. *The Cryosphere* **17**(5), 1967-1987. https://doi.org/10.5194/tc-17-1967-2023.

Woods T and Hewitt IJ (2024) Modelling the evolution of an ice sheet's weathering crust. *IMA Journal of Applied Mathematics*. https://doi.org/10.1093/imamat/hxae031.

Yang K, Smith LC, Andrews LC, Fettweis X and Li M (2022) Supraglacial drainage efficiency of the Greenland Ice Sheet estimated from remote sensing and climate models. *Journal of Geophysical Research: Earth Surface*, e2021JF006269.

Yang K, Smith LC, Karlstrom L, Cooper MG, Tedesco M, van As D, Cheng X, Chen Z and Li M (2018) A new surface meltwater routing model for use on the Greenland Ice Sheet surface. *The Cryosphere* **12**(12), 3791-3811. https://doi.org/10.5194/tc-12-3791-2018.

Žebre M, Colucci RR, Giorgi F, Glasser NF, Racoviteanu AE and Del Gobbo C (2021) 200 years of equilibrium-line altitude variability across the European Alps (1901–2100). *Climate Dynamics* **56**(3), 1183-1201. https://doi.org/10.1007/s00382-020-05525-7.

Supplementary Information:
The formation and evolution of the supraglacial weathering crust on the Greenland Ice Sheet

Ian T. Stevens[1,2], Joseph M. Cook[1], Lou-Anne Chevrollier[1], Adam J. Hepburn[3], Alex M. Anesio[1], Liane G. Benning[4,5], and Martyn Tranter[1]*

Supplementary Table S1 | Specification of the AWS deployed at ILU-22.

Instrument	Manufacturer and Model	Resolution	Accuracy
Barometer	HOBO S-BPB-CM50	0.01 hPa	± 3 hPa
Hygro-thermometer (temp)	HOBO S-THC-M002	0.02 °C	± 0.25 °C
Hygro-thermometer (RH)	HOBO S-THC-M002	0.01%	± 2.5% ± 5% when 10% < RH < 90%
Anemometer (speed)	HOBO S-WSB-M003	0.5 m s^{-1} (minimum 1.0 m s^{-1})	± 1.1 m s^{-1} or 4% (whichever is greater)
Anemometer (direction)	HOBO S-WDA-M003	1.4° (minimum 1.0 m s^{-1})	± 5°
Radiometer	Kipp and Zonen CNR4	< 1 W m^{-2}	± 10%

All sensors were manufacturer calibrated prior to deployment in 2022.

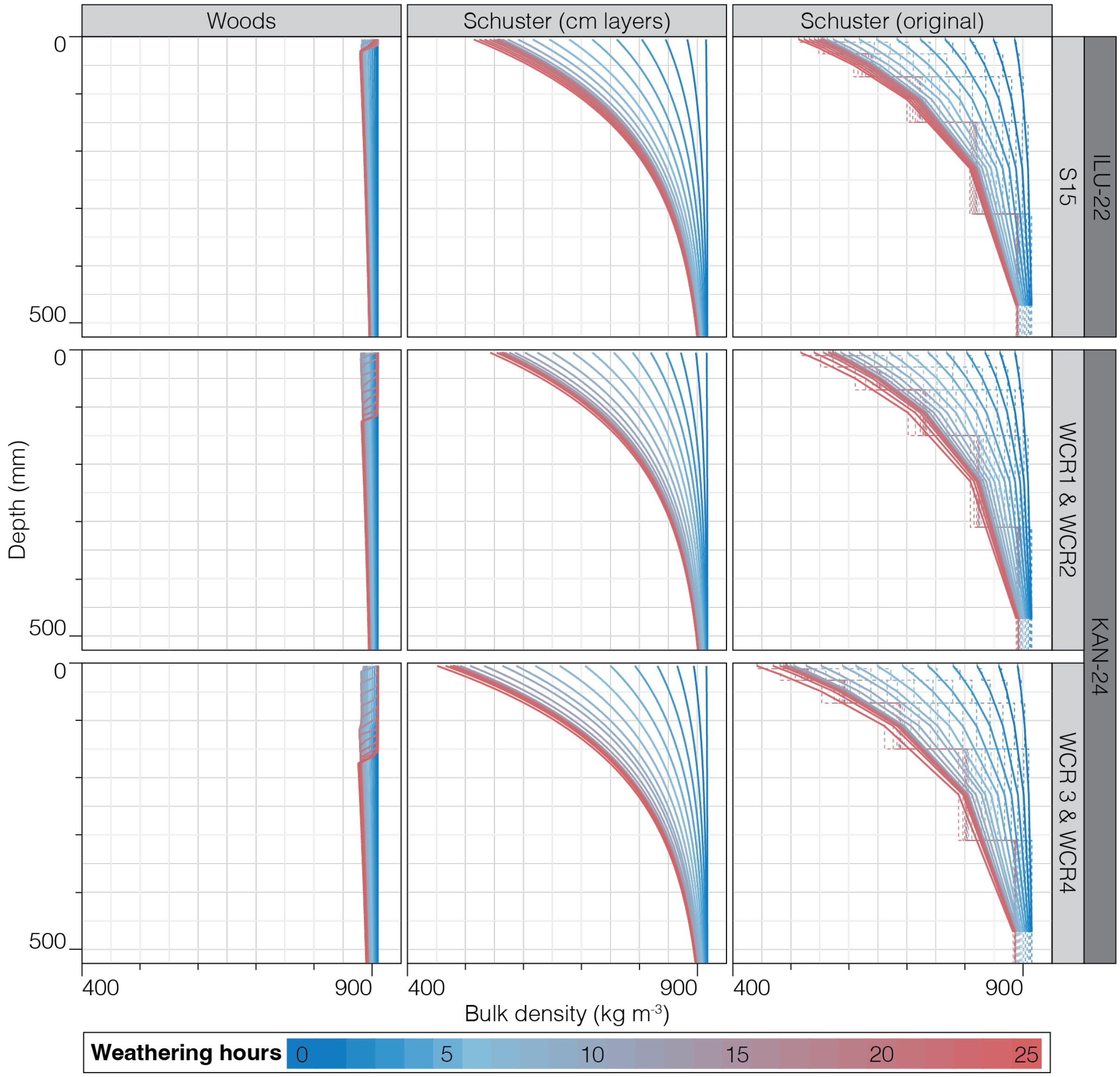

Supplementary Figure 1 | Modelled weathering crust reset experiments, showing change in ice density (y axis) across the depth profile (x axis), over time (line colour). The Woods model was run on a one minute timestep (i.e. the default setting). The Schuster model was run on a both 300 second and one-hour timestep – when the 300 second interval was resampled using an hourly timestep, the depth density curves were identical. The Woods model was run using the default 0.01 m core segment thickness, and Schuster model was also run using both a 0.01 m core segment thickness (centre), and in its original format (right) using 6 core segments of 2^n m thick, where $0 \leq n \leq 5$. The direct output from the model runs are shown using dashed lines, and interpolated with solid lines. As for the timestep variations, there is no difference in the output data when using each core segment thickness configuration. Note WCR 1 & WCR2 are shown together, as are WCR3 & WCR 4, given the matching weather conditions during these experimental periods.

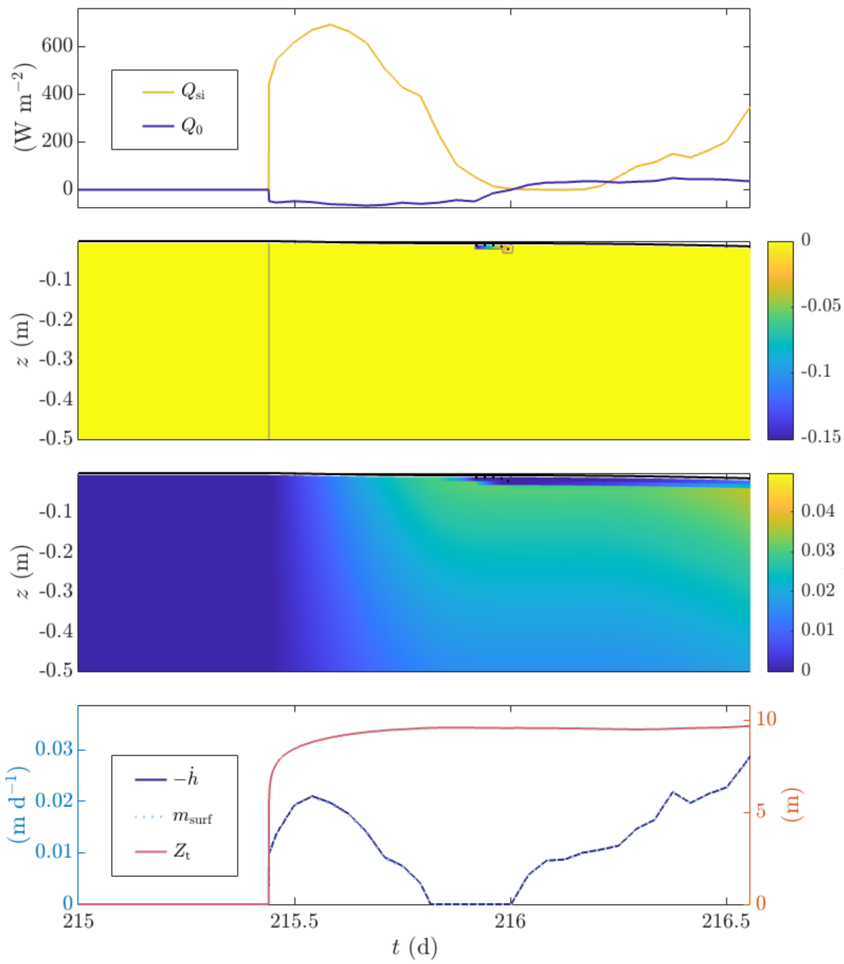

Supplementary Figure 2 | Direct output from the Woods (2024) model for S15. From top-to-bottom, the panels show: i) energy fluxes (i.e. model input), ii) modelled ice temperature, iii) pore space occupied by water (converted to bulk density via Equation 5 in the main manuscript), and iv) surface lowering (-h, left axis) and weathering crust depth (Z_t, right axis).

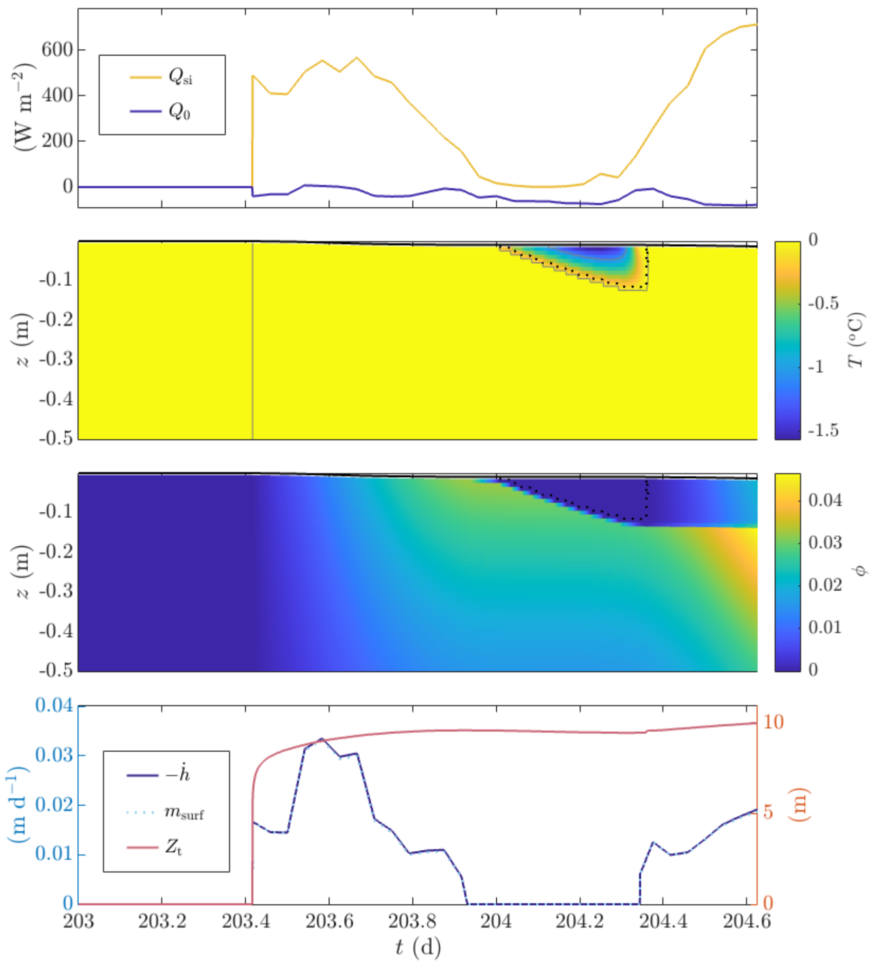

Supplementary Figure 3 | Direct output from the Woods (2024) model for WCR1. From top-to-bottom, the panels show: i) energy fluxes (i.e. model input), ii) modelled ice temperature, iii) pore space occupied by water (converted to bulk density via Equation 5 in the main manuscript), and iv) surface lowering (-h, left axis) and weathering crust depth (Z_t, right axis).

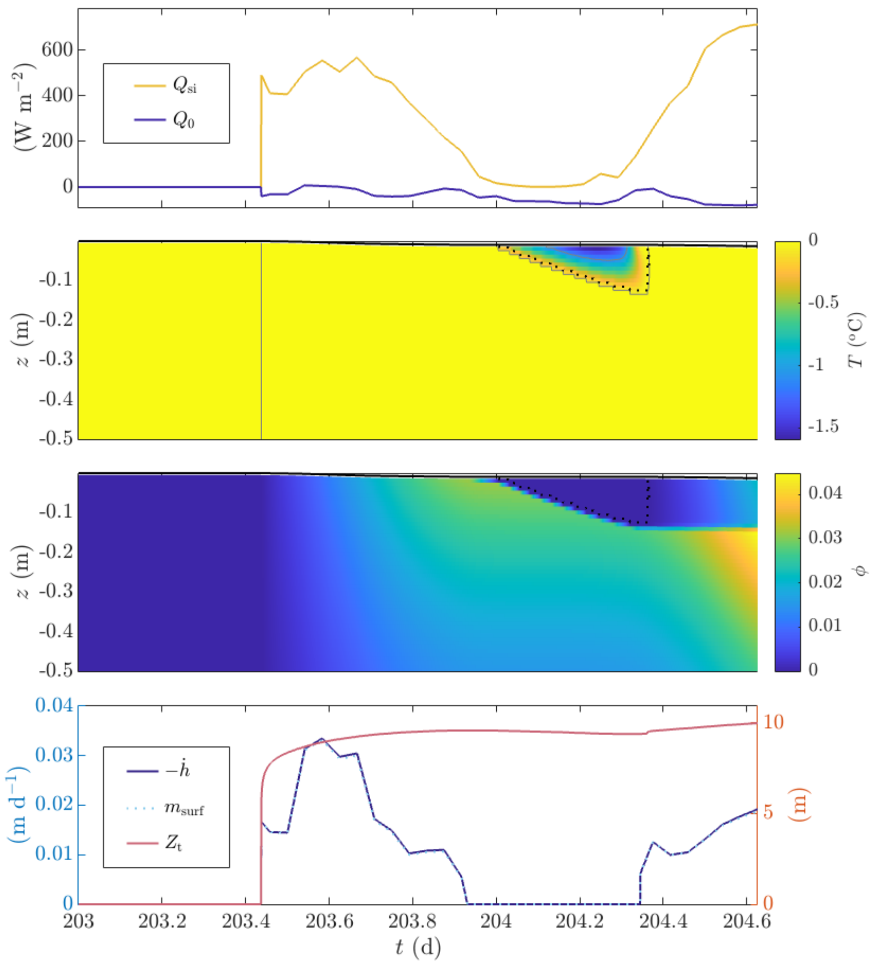

Supplementary Figure 4 | Direct output from the Woods (2024) model for WCR2. From top-to-bottom, the panels show: i) energy fluxes (i.e. model input), ii) modelled ice temperature, iii) pore space occupied by water (converted to bulk density via Equation 5 in the main manuscript), and iv) surface lowering (-h, left axis) and weathering crust depth (Z_t, right axis).

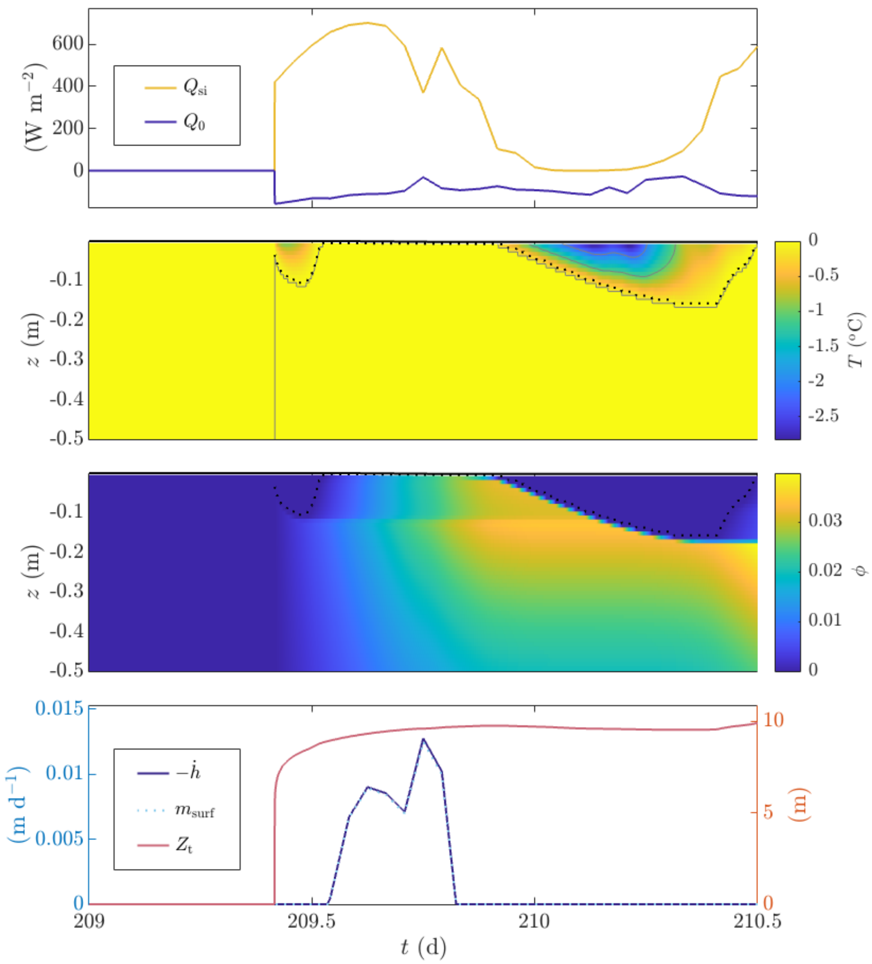

Supplementary Figure 5 | Direct output from the Woods (2024) model for WCR3. From top-to-bottom, the panels show: i) energy fluxes (i.e. model input), ii) modelled ice temperature, iii) pore space occupied by water (converted to bulk density via Equation 5 in the main manuscript), and iv) surface lowering (-h, left axis) and weathering crust depth (Z_t, right axis).

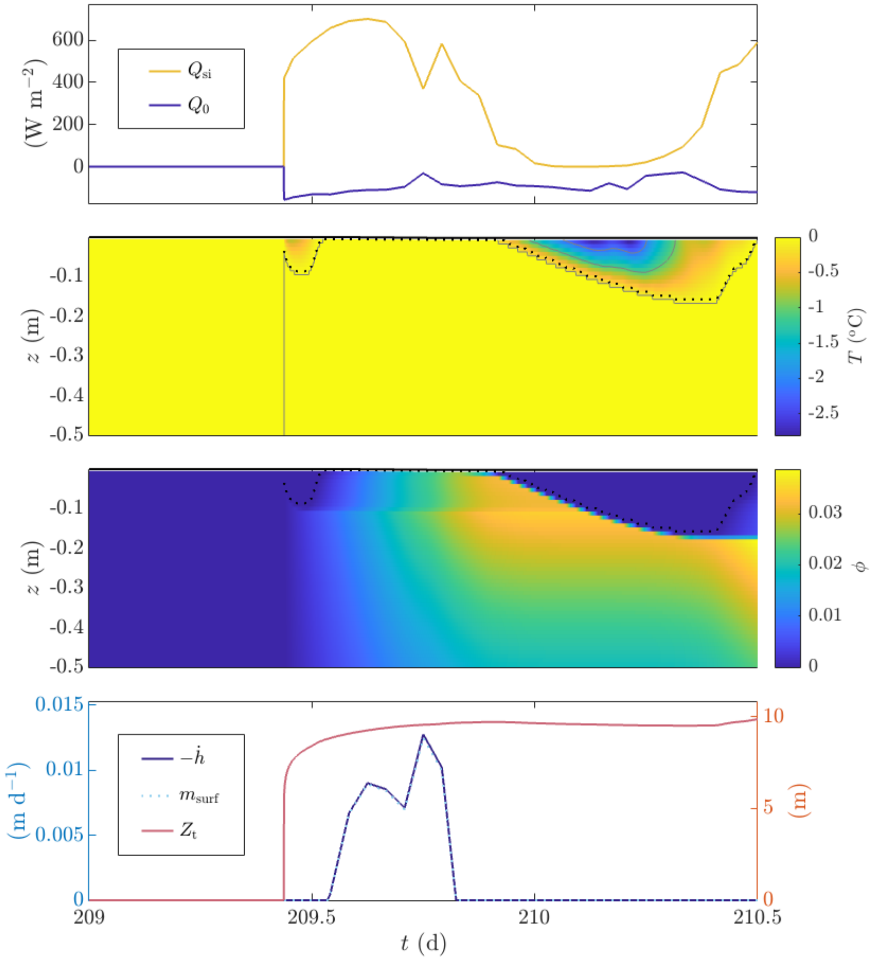

Supplementary Figure 6 | Direct output from the Woods (2024) model for WCR4. From top-to-bottom, the panels show: i) energy fluxes (i.e. model input), ii) modelled ice temperature, iii) pore space occupied by water (converted to bulk density via Equation 5 in the main manuscript), and iv) surface lowering (-h, left axis) and weathering crust depth (Z_t, right axis).

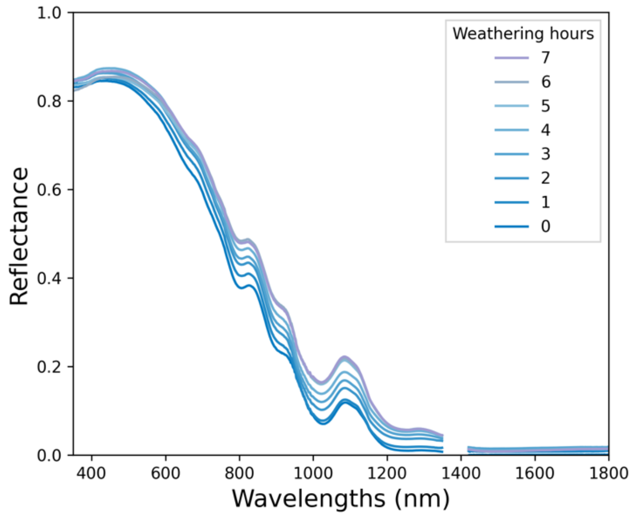

Supplementary Figure 7 | Surface reflectivity at S15, for the 7 timepoints surrounding solar noon.